nature geoscience

SUPPLEMENTARY INFORMATION

DOI: 10.1038/NGEO2954

In the format provided by the authors and unedited.

The hottest lavas of the Phanerozoic and the survival of deep Archaean reservoirs

Jarek Trela, Esteban Gazel, Alexander V. Sobolev, Lowell Moore, Michael Bizimis, Brian Jicha and Valentina G. Batanova

Background and classification of the Tortugal Suite melts

The Tortugal Suite is located on the western coast of Costa Rica, east of the Gulf of Nicoya (Fig. S1A-C). This terrane occurs within the Nicoya Complex that represents the westernmost extent of the Caribbean Plateau. These lava flows occur as isolated mounds along a narrow 12 km stretch striking ~N 65° W (Alvarado et al., 1997). Ar-Ar dating on alternation-free chips yielded a mean age plateau of 89.86 ± 4.73 (Table S1). This age is consistent with the one reported in (Alvarado et al., 1997).

Only two previous studies of accreted Galapagos plume-related terranes discuss the geology of Tortugal picrites and basalts in detail. Alvarado et al. (1997) first suggested that the Tortugal Suite should be classified as a komatiite locality, largely based on the major element chemistry of whole rock samples and occurrences of acicular pyroxene texture resembling "microspinifex". This study also used petrological modeling based on major element chemistry to infer initial melting at 1700 °C and at a depth of ~150 km (~5 GPa). Alvarado et al. (1997) also observed the presence of acicular olivine and pyroxene in thin-sections; an observation also supported by our study. The second study (Hauff et al., 2000) collected whole rock major, trace element, and radiogenic isotope for picrites and alkaline basalts from Tortugal, suggesting an "OIB-type" signature for this terrane.

Samples used in this study were collected from outcrops along roadsides and from the interiors of large (>1 m in diameter) boulders. GPS coordinates for all samples are provided in Table S2A. Our new whole rock analyses for 16 Tortugal samples reveal first-order petrological similarity to Archean komatiites. The Tortugal samples are high in MgO (27-34 wt.%) and FeO (11.0-12.6 wt.%) and low in TiO_2 (0.53-1.09 wt.%)(Table S2). The CaO/Al_2O_3 ratios of these samples range from 0.90 to 1.23. The Al_2O_3/TiO_2 ratios range from 4-10 and are subchondritic (<22) while $(Gd/Yb)_N$ range from approximately 1.4 to 2.8 (Fig. S2A). In this respect, Tortugal samples show an affinity to the classically defined Al-depleted Barberton komatiites as well as picrites from the Phanerozoic Emeishan Large Igneous Province. The high $(Gd/Yb)_N$ and low Al_2O_3 of the Tortugal samples indicate significant depletion in heavy rare earth elements (HREEs) and reflect an abundance of garnet in the residue post melting. This suggests relatively deep melt generation at pressures well with the garnet stability field (> 2GPa). Interestingly, there exists a decreasing trend in $(Gd/Yb)_N$ and Al_2O_3 with respect to other Galápagos LIP localities (Curacao and Gorgona).

Perhaps a more intuitive way to compare the major element similarity of Tortugal samples to Archean komatiites is by using a plot developed by Eero Hanski (Hanski, 1992). This approach is useful in demonstrating the covariation of Al_2O_3 and TiO_2 contents of various ultramafic lavas. The major benefit of this approach is that it projects liquid compositions from olivine and eliminates the effects of olivine fractional crystallization that provides a direct comparison of liquids with variable MgO contents. Tortugal lavas plot within the Ti-enriched komatiite and picrite fields (Fig. S2B). These samples contain high TiO_2, similar to other high-MgO Phanerozoic

localities. Tortugal lavas plot within the dominant field of high MgO ELIP flows. Curacao and Gorgona lavas show markedly lower TiO_2 contents and display more similarity to Kambalda and Munro Al-undepleted and Al-enriched komatiites (Fig. S2B).

While our Tortugal lavas lack a macro-spinifex texture, they do contain isolated clusters of platy, elongated olivine and acicular pyroxene crystals with a distinct shape preferred orientation that microscopically resembles classic spinifex textures (Fig. S3A-B). The origin of this texture in the Tortugal samples is unclear. The samples have abundant olivine phenocrysts, and renders undercooling as an improbable process. It stands possible that these samples retain some memory of an earlier supercooled state (Lofgren, 1983) overprinted by serpentinization and hydrous alteration of primary phenocrysts (Alvarado et al., 1997).

The main feature that separates komatiite from other types of high-MgO ultramafic rocks is the occurrence of macroscopic spinifex textures (Kerr and Arndt, 2001). Our Tortugal samples only exhibit acicular texture in some samples (a photo album of this texture is available upon request from the corresponding author). Therefore, this suite should therefore be classified as picritic.

Evidence for the phenocrystic origin of high-Mg Tortugal olivines

Tortugal olivines are unique relative to other hotspot related terranes with respect to their high Mg# (molar Mg/(Mg+Fe)*100) that reach values up to 94.2, systematically overlapping those of Archean komatiites (Fig. 1B). These olivines are phenocrysts as evidenced by their high calcium, chromium, aluminum, and titanium contents (relative to residual/lithospheric olivine), abundance of melt inclusions in the most forsteritic olivine, and normal magmatic zoning from core to rim (see Supplementary Information for detailed chemical maps and images of these features). The high contents of Ca, Cr, and, Al of Tortugal high-Mg olivines and the presence of melt inclusions preclude their origin form disintegrated lithospheric xenoliths. Petrologic modeling indicates that these phenocrysts crystallized from a hot, primary peridotite melt and their Ni contents are consistent with derivation from a hot, deep primary melt with ~27 wt.% MgO (Fig 2A), indicative of initial high pressure and temperature melting.

These key observations indicate a phenocrystic origin for Tortugal olivines:

Tortugal olivines are unique relative to other mantle plume related terranes with respect to their high Mg# (molar Mg/(Mg+Fe)*100) that reach values up to 94.2, systematically overlapping those of Archean komatiites (Fig. 1B).

These key observations indicate a phenocrystic origin for Tortugal olivines:

1) The olivines contain melt inclusions including the magnesium rich olivines (Fo94). Two of the melt inclusions analyzed for volatile concentrations are also included in the high magnesium olivine (Fo93). We have included transmitted and reflected light images as an Atlas (provided below)as

evidence for these olivines crystallizing from a melt.

2) Chemical mapping of these olivines indicates a gradual chemical zonation from core to rim and being more primitive at their cores. Several chemical maps are included in the Atlas below.
3) Additional reflected light images of spinel inclusions inside Tortugal olivine phenocrysts have also been added to the Atlas.
4) Tortugal olivines have high Ca, Ti, and Al concentrations. These concentrations are higher than residual (lithospheric) olivines (e.g., (Foley et al., 2013), Fig. 2). See Figure S4 for comparison.
5) Petrologic modeling indicates that these phenocrysts crystallized from a hot, primary peridotite melt and their Ni contents are consistent with derivation from a hot, deep primary melt with ~27 wt.% MgO (Fig 2A), indicative of initial high pressure and temperature melting.

Trace element and isotope systematics

Archean and Gorgona island komatiites commonly display depleted chondrite-normalized rare earth element (REE), however, Tortugal samples are unique in this regard because they display enriched light/heavy (LREE/HREE) patterns (Fig. S5). Also, Tortugal samples are enriched in trace elements compared to other CLIP high-MgO locations. Tortugal lavas also exhibit enriched trace element patterns with enrichments in high field strength elements (HFSE, e.g., Nb, Ta, Ti) and depletions in more fluid mobile elements (e.g., K, Sr, Pb) as observed in typical OIB localities, which strongly suggests an intraplate origin. Gorgona samples have the widest range in depleted incompatible trace elements. The nature of Gorgona lavas is best explained by variations in the degree of fractional melting [Arndt et al., 1997].

In terms of trace element enrichment, the Tortugal suite compares with other high-MgO Phanerozoic lavas, displaying similar REE patterns to the high MgO Emeishan Large Igneous Province (ELIP), though not as enriched as Siberian meimechites (Fig. S5B). This enrichment can best be explained by 1) low degrees of partial melting of a fertile peridotite (e.g., (Hofmann, 1997) or 2) partially melting an enriched mantle source (e.g., (Harpp and White, 2001) or 3) partial melting of a hydrous or carbonated source (e.g., (Dasgupta et al., 2007). We think that interpretations 1 and 3 are not consistent with the petrologic record of high MgO melts and komatiites (Herzberg, 1992). Additionally, we find little similarity between Tortugal and experimentally derived carbonated peridotite primary melts (see below). Our volatile assessment also suggests a source poor in hydrous phases. Melted recycled crust embedded within partially melted peridotite might help to explain the trace element and radiogenic isotope mixing lines. Melt inclusions also show a range of TiO_2 concentrations that strongly correlate with K_2O. We used the strong correlations between TiO_2 and rare earth elements to model the trace element concentrations of primary melts with variable amounts of TiO_2 (Fig. S6). These models further corroborate mixing between a low-Ti (< 0.5 wt.%), trace element depleted source and a high-Ti (~1.2 wt.%), trace element enriched source. Although this enriched component probably refertilized the peridotite matrix, it did not overcome the composition to complete turn it into an olivine-free source.

Age corrected radiogenic isotope ratios reveal that Tortugal samples are enriched in radiogenic $^{206}Pb/^{204}Pb$ and $^{208}Pb/^{204}Pb$ and display unradiogenic $^{143}Nd/^{144}Nd$ signature (Fig. S7A-C). These samples show similarity to the classically defined Northern Galapagos isotopic Domain (Harpp and White, 2001) with some overlap the Central Domain that is thought to represent the most pristine "plume component"(Harpp and White, 2001). More importantly these samples tend to have high $^{207}Pb/^{204}Pb$ (15.55-15.60) that strongly overlaps lavas from the Wolf-Darwin Lineament of the Northern Domain. This anomaly is defined as having high $^{235}U/Pb$ and Th/U to account for the relative enrichments in $^{207}Pb/^{204}Pb$ and $^{208}Pb/^{204}Pb$ at a given $^{206}Pb/^{204}Pb$ (Harpp and White, 2001). Previous studies suggested that this isotopic reservoir originated early in Earth's history and was modified by subduction of either 1) sediments (Dupré and Allegre, 1983), 2) oceanic crust (Hart, 1984), or 3) delaminated subcontinental lithosphere (Hart, 1984). We favor the interpretation that recycled delaminated subcontinental lithosphere and re-entrainment into the plume or limited recycled oceanic crust in the plume. This is supported by the olivine chemistry of Tortugal samples as these data does not support a dominant pyroxenite source (i.e., high Ni and Fe/Mn and low Ca) as observed in other Galapagos related terranes (e.g. Quepos (Trela et al., 2015).

Assessment of volatiles in Tortugal samples

In this section we summarize the lines of evidence in the hydrous vs. anhydrous melting debate for the generation of picrites, komatiites and other high-MgO lavas. Grove et al. (1999) and Parman et al. (2001) championed the idea that komatiite melts formed during hydrous (metasomatized) mantle melting above a subduction zone. The main effect of adding water to the mantle is to decrease the solidus, and thus reduce melting temperatures to more "normal" levels. According to this model, boninites are modern equivalents of Archean komatiites, nevertheless the typical arc geochemical signatures evident in boninites are absent in Archean and Phanerozoic komatiites (Arndt, 2003). Therefore, the most accepted petrological model suggests that komatiites form via adiabatic decompression melting of relatively anhydrous and anomalously hot mantle plumes (Arndt, 1999; Berry et al., 2008; Herzberg, 1992; Walter, 1998).

We compared calculated major element primary melt compositions from Tortugal and other high-MgO samples with the experimentally derived primary melts of (Dasgupta et al., 2007). Figures S8A-D clearly show that the major element compositions of Tortugal samples are inconsistent with being derived from a carbonated peridotite source. The primary melts from the Dasgupta (Dasgupta et al., 2007) experiments show a strong negative correlation between CaO/Al_2O_3 and Al_2O_3/TiO_2. Primary melts from a non-carbonated source show very little variation in CaO/Al_2O_3 over a wide range of Al_2O_3/TiO_2. Likewise, the experimental carbonated primary melts plot along a well-constrained trend of increasing TiO_2/Al_2O_3 and CaO/Al_2O_3. Primary melts of non-carbonated sources also plot along a well constrained trend, however, the CaO/Al_2O_3 of these melts does not increase as drastically with increasing TiO_2/Al_2O_3 as do the carbonated peridotite primary melts. Finally, primary melts from volatile-poor sources plot along a tight, negative trend when CaO/(CaO+MgO) vs. MgO are plotted. This plot reveals that the

dominant effect of melting a carbonated peridotite source is to significantly increase CaO/(CaO+MgO) at any given MgO content. These simple major element diagrams are robust and practical tools for highlighting the differences between carbonated peridotite primary melts and volatile-poor primary melts.

In order to determine the CO_2 content of Tortugal lavas, we analyzed melt inclusions from sample TO-080714-8. Because melt inclusions often contain a mixture of glass and fluid that has exsolved from the melt after the inclusion has been trapped, we used a combination of secondary ion mass spectrometry (SIMS) and Raman spectroscopy following the method described by (Moore et al., 2015). We note that because the solubility of CO_2 sensitive to changes in pressure, it is possible that some of the CO_2 has been lost due to degassing of the melt before the inclusions were trapped, and thus the CO_2 contents reported in this study represent minimum values. Melt inclusions in olivine from all Tortugal lava samples were completely recrystallized, so it was necessary to experimentally reheat them. Separated olivine grains were heated to 1300 ^{o}C in vertical heating stage at oxygen fugacity corresponding to QFM buffer at Vernadsky Institute of Geochemistry, Russian Academy of Science, Moscow. Olivine grains were quenched after exposure of 5 minutes at top temperature. Grains were grinded and polished to expose inclusions on the surface. Exposed inclusions were then measured by EPMA, SIMS, and Raman spectroscopy (see Methods section for details).

Because it is possible for melt inclusions to trap a mixture of melt and exsolved vapor, we compared melt inclusion volumes and vapor bubble volumes to identify inclusions with anomalously large bubbles that may have been trapped heterogeneously. Figure S9A shows this comparison. One inclusion contains 22% vapor by volume and is significantly larger than the other inclusions; we interpret this inclusion to have trapped a mixture of melt + fluid, and we omit it from further interpretation. Other than this exception, there is a good correlation between MI volume and bubble volume, so the other inclusions likely contain bubbles that formed after trapping. Melt inclusions from sample TO-080714-8 contain vapor bubbles that range in size from 2 to 13 volume percent vapor with densities from 0 to 0.22 g/cm^3. This corresponds to melts with CO_2 contents ranging from 0 to 1 wt% CO_2 in the bubble (10,000 ppm in Figure S9B). Although this calculation does not account for additional CO_2 in the glass, the range of CO_2 contents calculated by analyzing bubbles only is generally consistent with the range of CO_2 contents that include analyses of the glass (Moore et al., 2015) (Hartley et al., 2014).

To correct for the effect of postentrapment crystallization (PEC), we performed petrological modeling of the olivine hosted melt inclusions to calculate the melt composition in equilibrium with the host olivine. During cooling, a trapped melt inclusion will crystallize olivine along the outer wall of the inclusion. This crystallizing rim will be progressively depleted in Mg and enriched in Fe. This results in a compositional gradient in the olivine adjacent to the inclusion, which can result in the diffusion of Fe out of and Mg into the original melt inclusion. To correct for "Fe-loss" and PEC we used Petrolog v.3 (Danyushevsky and Plechov, 2011). We ran several models (results provided in Table S2E) with varying oxidation states and olivine crystallization models. We assume a Fe^{2+}/Fe^{Tot} in the melt to be ~0.9 based on spinel compositions and following the approach of Danyushevsky and

Sobolev (1996) and assumed the FeO* content of the trapped melt to be ~11 (the average FeO* content of the whole rock samples). S concentrations are also low (max 995 ppm S at max H_2O content, see below) which suggests a relatively reduced primary melt (Gazel et al., 2012). Furthermore, the V/Sc ratio of Tortugal picrites is 5.42 ± 0.57 (1σ). The V/Sc ratios of these picrites are comparable to modern mid-ocean ridge basalts (6.74 ±1.11, 1σ) and Archean basalts (6.34 ± 0.62, 1σ) indicating that the fO_2 of the mantle source for these melts to be at least 0.3 ± 0.5 (1σ) log units below the Quartz-Fayalite-Magnetite (QFM) buffer (Li and Lee, 2004). Our models suggest ~17 wt% MgO for melts in equilibrium with their host olivine. This value is highly dependent on the 1) olivine crystallization model we use and 2) the initial oxidation state. Additionally, from all of the prepared and analyzed melt inclusions we were unsuccessful in finding reheated trapped melts in the highest Mg# olivine range (e.g., >94). The highest Mg# of the host olivine where we found reheated melt inclusions was 93.13. The highest MgO content was obtained when using the model of (Herzberg and O'Hara, 2002) and an oxidation state controlled by a QFM buffer. This produced melts with up to 23 wt% MgO, approaching our PRIMELT3 results that yielded MgO contents of approximately 27 wt% MgO. Future studies will focus on a larger population of re-equilibrated olivine hosted melt inclusions trapped in the most primitive olivine phenocrysts having Mg#s > 93.

Effect of volatiles on mantle potential temperature calculations

Any estimation of mantle potential temperature must take several variables into account, namely an assessment of volatiles (CO_2 and H_2O) and the redox state of the mantle source. The uncertainty in both of these variables can lead to significant variability in the estimated mantle potential temperature. For example, the cryoscopic effect (the change in the temperature of the solidus, liquidus, or melting isopleth upon addition or subtraction of volatiles) when adding H_2O is approximately a 100 °C decrease for every 3.5 wt% addition of H_2O (Tenner et al., 2012). The cryoscopic effect of CO_2 is approximately 3 times less than that of H_2O (Tenner et al., 2012). This means that it would take 12 wt.% CO_2 to produce the same a 100 °C depression.

The maximum water content in the melt inclusions is 0.24 wt% and the average H_2O/Cl ratio is ~11. Because there is a possibility that our melt inclusions lost H_2O due to H^+ diffusion, we can use the H_2O/Ce (Dixon et al., 2002) and CO_2/Nb (Michael and Graham, 2015) ratios of Pacific OIBs (200 and 1029 ppm, respectively) with the maximum Ce and Nb values from Tortugal samples (Table S2A) as another proxy for volatile concentrations. Using this approach, we find that Tortugal melts could be consistent with a maximum of 0.5 wt.% H_2O and 1.6 wt% CO_2. Assuming these as representative values of H_2O and CO_2, it will result in a ~50 °C decrease(Herzberg, 2016) in the T_p calculation, lowering the T_p maxima from 1803 to 1753 °C (close to the actual uncertainty of T_p of ±50 °C (Herzberg and Asimow, 2015). If we use the maximum Ce and Nb values for Tortugal from Table S2A, then we obtain 0.6 wt.% H_2O and 2 wt.% CO_2 for Tortugal melts. The range of our H_2O calculations (0.4-0.6 wt.%) is consistent with our measurement of olivine-hosted melt inclusions that suggested a maximum H_2O content of 0.24 wt.%. Our CO_2 estimates range from 1.6-2 wt.%; the upper limit being slightly higher than our

measured MI+vapor concentration of 1.6 wt.%. Using these as minimum values of H_2O and CO_2, this will result in a ~22 °C decrease in the T_p calculation. Therefore, our hydrated T_p estimates range from 1753 to 1781 °C (± 50 °C). Our mantle potential temperatures, along with the high Al-in-olivine crystallization temperatures, support hot and relatively dry conditions for the generation of these lavas.

Quantifying the amount of melt produced at high MgO komatiite or picritic P-T melting conditions remains problematic. One significant limitation to our petrologic modeling is that methods such as PRIMELT3 are not parameterized to estimate melt fraction (F) at such extreme P-T conditions (Herzberg and Asimow, 2015). However, using the approach of (Putirka et al., 2007), we estimate F to be ~30% for Tortugal melts. This value is also obtained when using the graphical approach of (Sossi et al., 2016) that is based on the Al_2O_3 and Al/Ti of high MgO melts. Additionally, Tortugal whole rock compositions plot in the same space as the classic Barberton aluminum-depleted komatiite type supporting F to be ~30%.

Extended Petrological Modeling Methods

Based on our geochemical data and petrologic modeling we are confident that Tortugal melts originated through hot, deep melting (most likely the hot axis of the Galapagos mantle plume) of a peridotite source as well as a recycled component enriched in trace elements. There is good agreement between our Al-in-olivine temperatures and estimated T_p based on whole rock compositions. To demonstrate this, we re-estimated T_p using equation 17 from Herzberg and Asimow (2015)(Figure S11) and compared these results with our initial estimates based on whole rock compositions. This equation is based on the idea that high MgO primary melts should also crystallize olivines with high liquidus temperatures. Figure S11A shows the results of estimating T_p based on the highest Al-in-olivine temperature that we obtained for each sample. Figure S11B shows the relationship between olivine crystallization temperatures using Al-in-olivine thermometry and olivine-liquidus temperatures (eq. 13, Herzberg and Asimow, 2015) using modeling primary melt compositions from PRIMELT3. The highest temperature Al-in-olivine data points fall on the 1:1 correlation line, suggesting good internal consistency between two independent thermometers. The off-set to lower Al-in-olivine temperatures is most readily attributed to fractional crystallization and mixing between the two end member Tortugal melts.

One critical aspect of our data that must be considered is the relationship between olivine and spinel liquidus temperatures. In recent experiments (Sobolev et al., 2015) it was found that the maximum crystallization temperature of spinel was 1550 °C. This value is 50°C lower than the maximum Al-in-olivine crystallization temperature for Tortugal. We performed petrologic modeling to explore the relationship between pressure on the liquidus temperature of spinel in an effort to reconcile the disconnect between the experimental observations and our empirical calculations. We used rhyolite-MELTS v. 1.2.0 (Gualda et al., 2012) and a pressure range of 0-2 GPa. We used the primary melt composition from TO-080614-8 as the initial composition. We found pressure to be a dominant factor, i.e., spinel crystallization is stabilized at higher pressures (Fig. S13). At ~0.5 GPa the spinel-

liquidus intersects the olivine-liquidus and at higher pressures, spinel is the first phase to crystallize from a Tortugal primary melt. Our models, together with the high stabilization temperature of spinel, suggest that Tortugal olivines began crystallizing at lithospheric depths between 0 and 0.5 GPa. It is important to note that although the modeled liquidus temperature increases with pressure, results from the Al-in-olivine thermometer show no pressure dependence on temperature. Additionally 0.5 GPa, the olivine-liquidus temperature is 25 °C higher than the 1 atm liquidus-temperature, and thus, still within the error of the Al-in-olivine thermometer (±30 °C).

Other anomalously hot LIP and OIB Phanerozoic localities (Emeishan, Iceland, Hawaii) have the potential to preserve melt from the plume core. A recent geodynamic study (Andrault et al., 2016) suggested a 4.3 Ga steady-state thermal scenario for the lowermost mantle, the D'' layer. If plumes do in fact "tap" the hot D'' layer that has not appreciably cooled over 4.3 Ga, then it stands to reason that even modern plumes can produce basaltic melts at similar T-P conditions as inferred during the Archean. Komatiites occurred more frequently during the Archean due to overall higher ambient mantle temperatures, though anomalously hot domains still exist in the deep portions of the planet and are only sampled by "true" plume core components (Fig. 12).

Application of Al-in-olivine thermometry to samples outside the calibration range

It is important to note that although Tortugal spinels have chromium contents higher than the calibrated range for the Al-in-olivine thermometer, there is a strong correlation (using the available global data) between K_d (Al_2O_3olivine/Al_2O_3spinel) and spinel chromium number (molar proportion of Cr/Cr+Al). Because the partition coefficient (K_d) increases proportionally (and with a statistical significance R^2=0.75) with increasing spinel Cr-number (Fig. S14), then we can conclude that olivines in equilibrium with the most Cr-rich spinels also provide meaningful temperature results. The application of this thermometer to olivine-spinel pairs of komatiites and low calcium boninites also outside the calibrated range yield temperatures within the errors of olivine-melt temperatures calculated from Fe-Mg and Sc/Y partition (Sobolev et al., 2016). Tortugal high-Mg olivines contain abundant micro-inclusions (from 20 μm down to few microns) of spinel, melt, and combined spinel and crystalized melt inclusions. This suggests that small spinel grains already coexisted with melt during crystallization of high-Mg olivines and allows applying of Al-in olivine- spinel geothermometer.

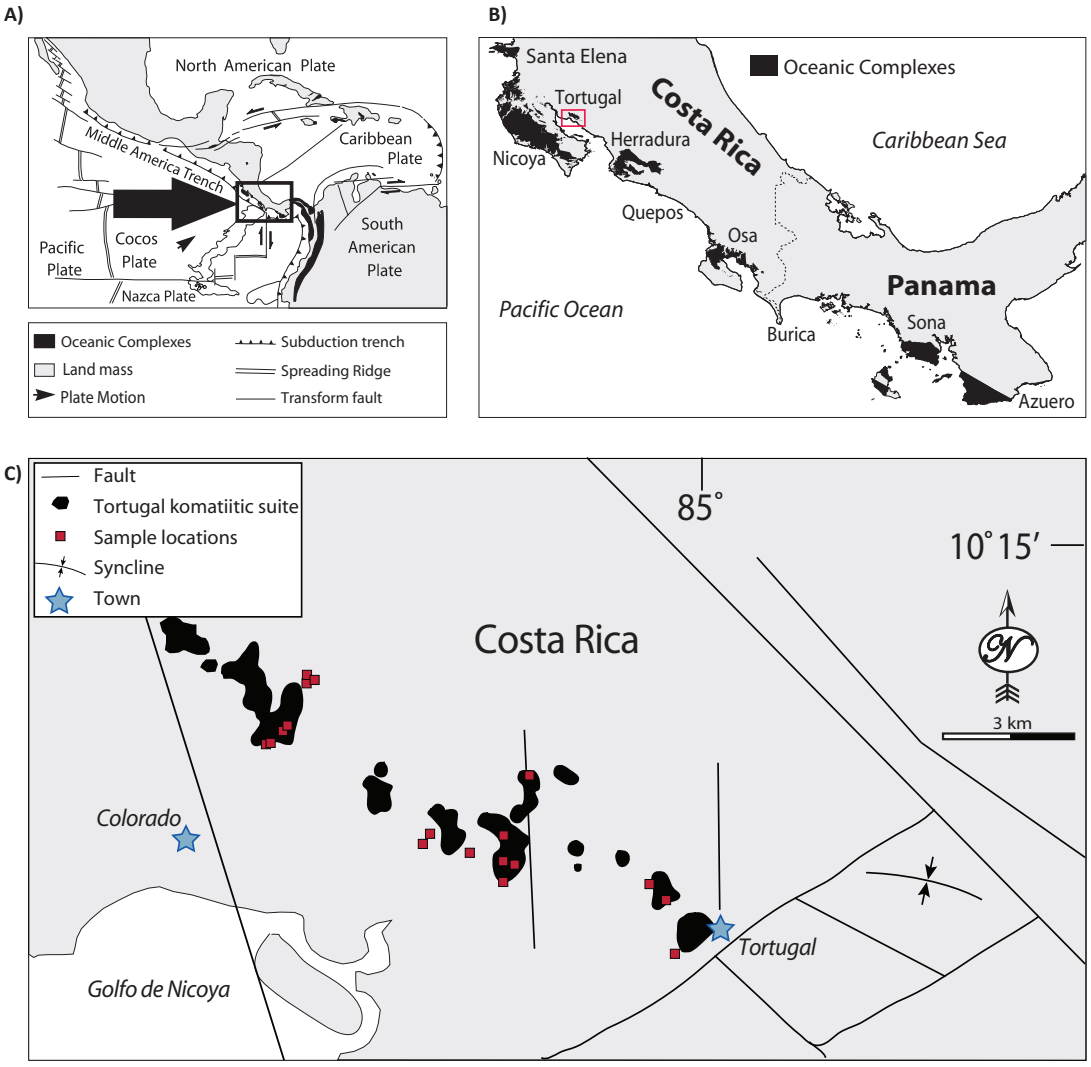

Figure S1: A) Tectonic location of the study area and Caribbean region (modified from Denyer and Gazel (2009)). B) Map showing accreted oceanic complexes along the west coast of Central America (modified from Denyer and Gazel (2009)). C) Simplified map of the Tortugal terrane denoting sample locations, and structures.

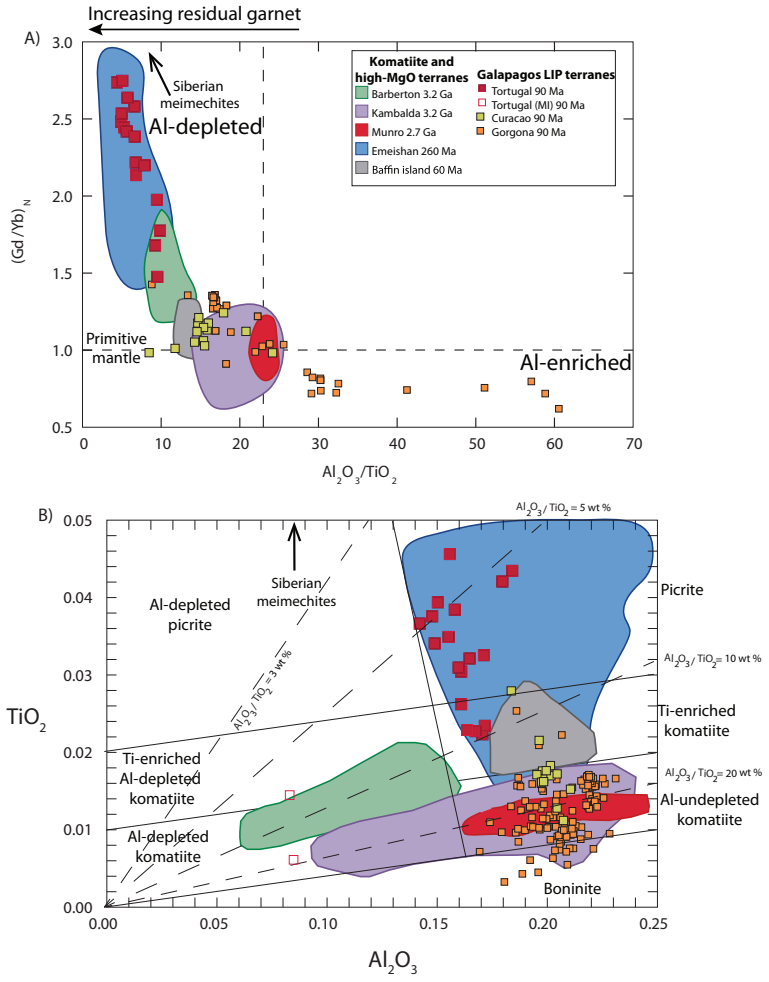

Figure S2: A) $(Gd/Yb)_N$ vs. Al_2O_3/TiO_2 where N=normalized to primitive mantle (McDonough and Sun, 1995). The dominant fields for Archean komatiites and high MgO Phanerozoic basalts are drawn using data from the GEOROC database. (http://georoc.mpch-mainz.gwdg.de/georoc/). B) Al_2O_3 vs. TiO_2 "Hanski" diagram for high MgO volcanic rocks from the CLIP (including reconstructed Tortugal melt inclusions), komatiites, and other high-MgO plume related terranes. Al_2O_3 and TiO_2 are in molar proportions and projected from the olivine composition using the following formulas: $Al_2O_3 = Al_2O_3/(0.67\text{-MgO-FeO})$ and $TiO_2 = TiO_2/(0.67\text{-MgO-FeO})$. See Hanski et al. 2001 for a detailed description of the method. Generalized fields for Archean komatiites include Barberton Al-depleted, Kambalda, and Munro. Primary magmas for all displayed data can be found in Table S2C. Fields for high MgO Phanerozoic lavas include the ELIP and Baffin Islands. Additional literature data is from the GEOROC database (http://georoc.mpchmainz.gwdg.de/georoc/). Data for Curacao and Tortugal samples is from this study.

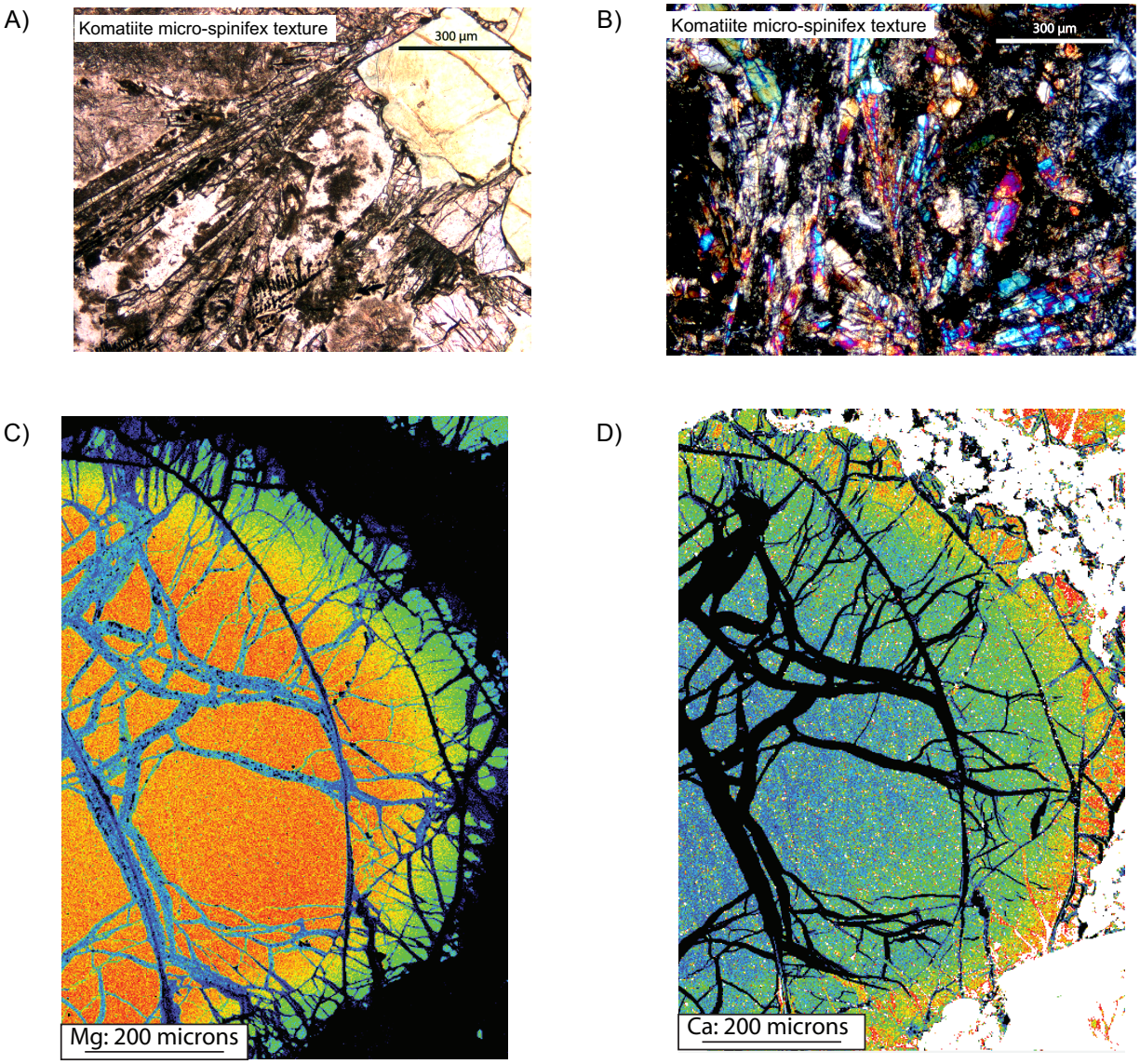

Figure S3: A) Acicular pyroxene textures found in Tortugal sample TO-010513-5 in plane polarized light. B) Acicular pyroxene textures found in Tortugal sample TO-010513-5 in cross polarized light. C) and D) Chemical maps of Mg and Ca, respectively, in a Tortugal olivine in thin-section showing normal magmatic zoning from core to rim.

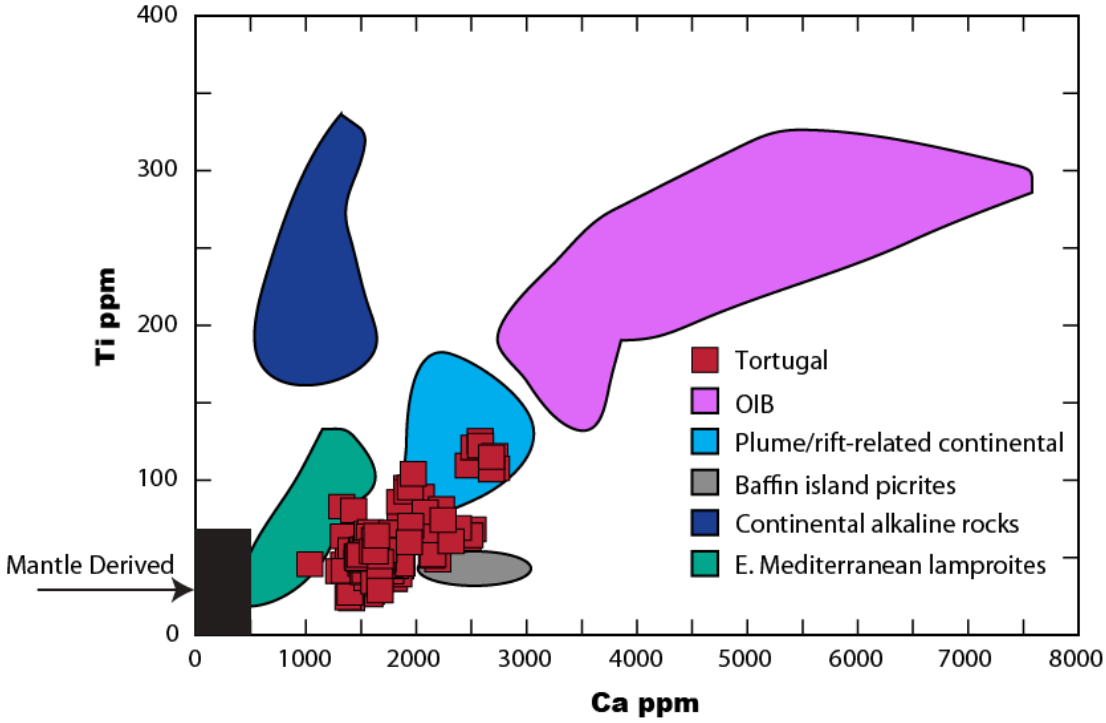

Figure S4: Calcium and titanium contents (in ppm) for volcanic olivine phenocrysts and residual lithospheric crystals. Volcanic phenocrysts are higher in Ti and Ca than in residual mantle olivine. Note that the Tortugal population overlaps volcanic populations that crystallized from a melt. Modified from figure 2 (Foley et al., 2013).

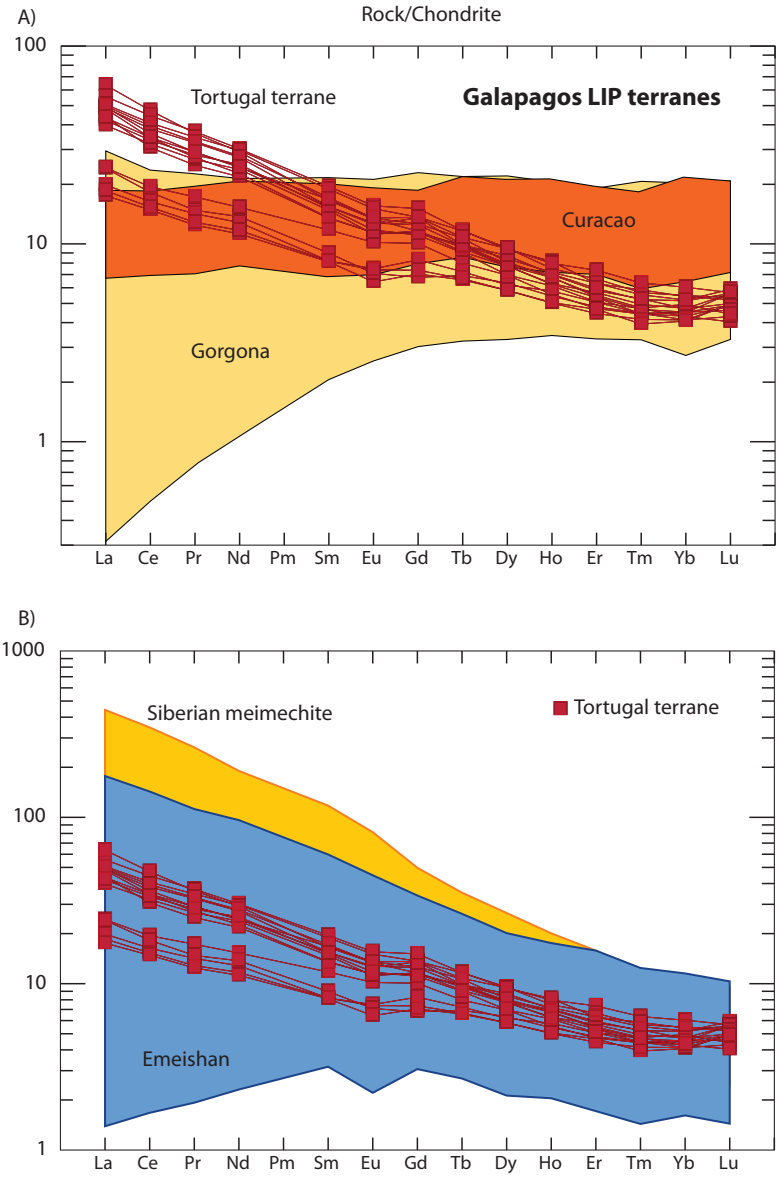

Figure S5: Chondrite normalized spider diagrams for high-MgO Galapagos related terranes (A) and the Siberian Traps and Emeishan Large Igneous Province (B).

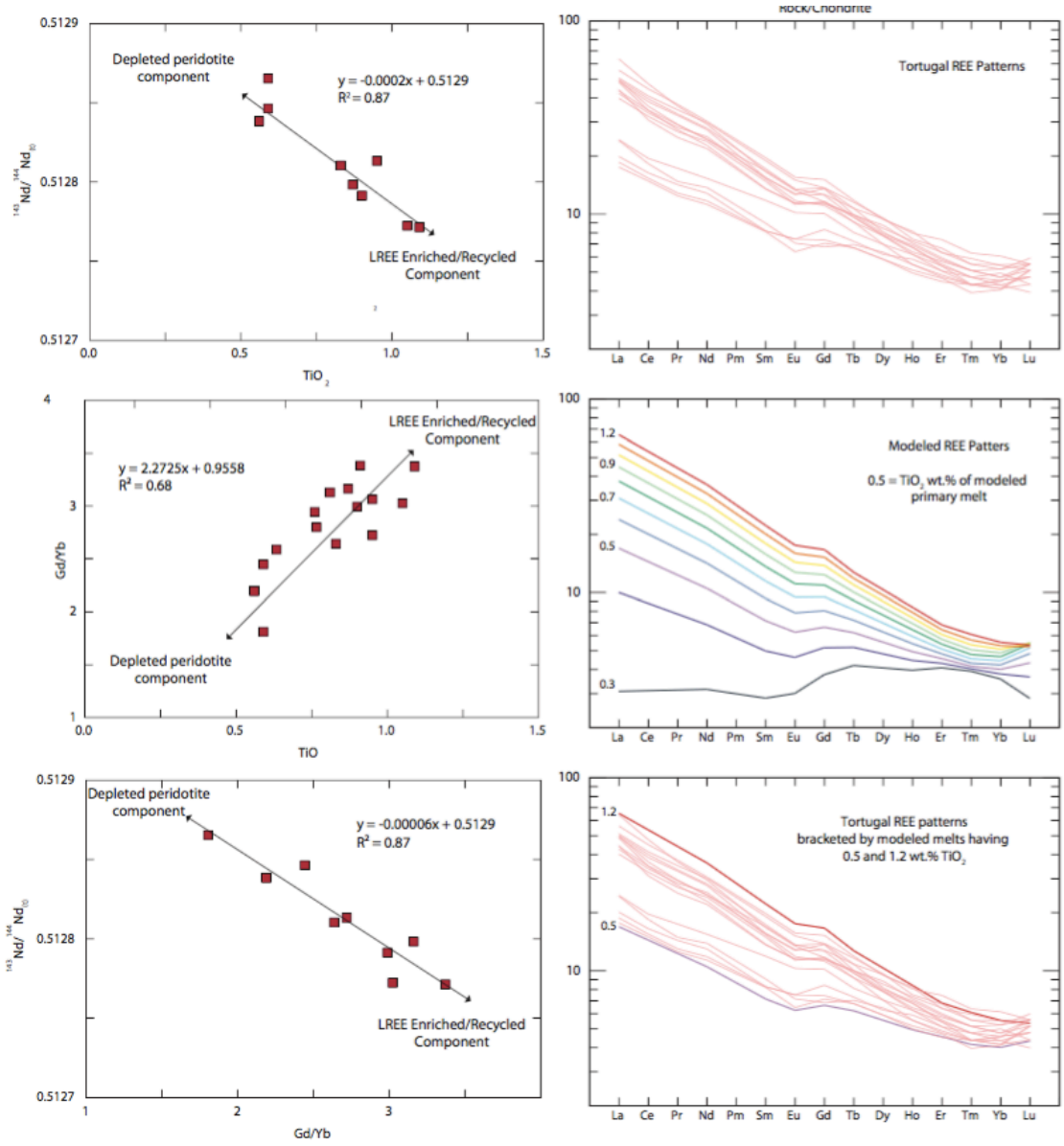

Figure S6: Correlations showing evidence of mixing between an enriched high-Ti melt and depleted low-Ti melt. Quantitative models for the rare earth element patterns. We used the strong correlations between TiO_2 and REE's to estimate the composition of primary melts as a function of TiO_2. Tortugal melts are likely to be mixtures between a low-Ti, depleted peridotite source and a high-Ti, enriched recycled component.

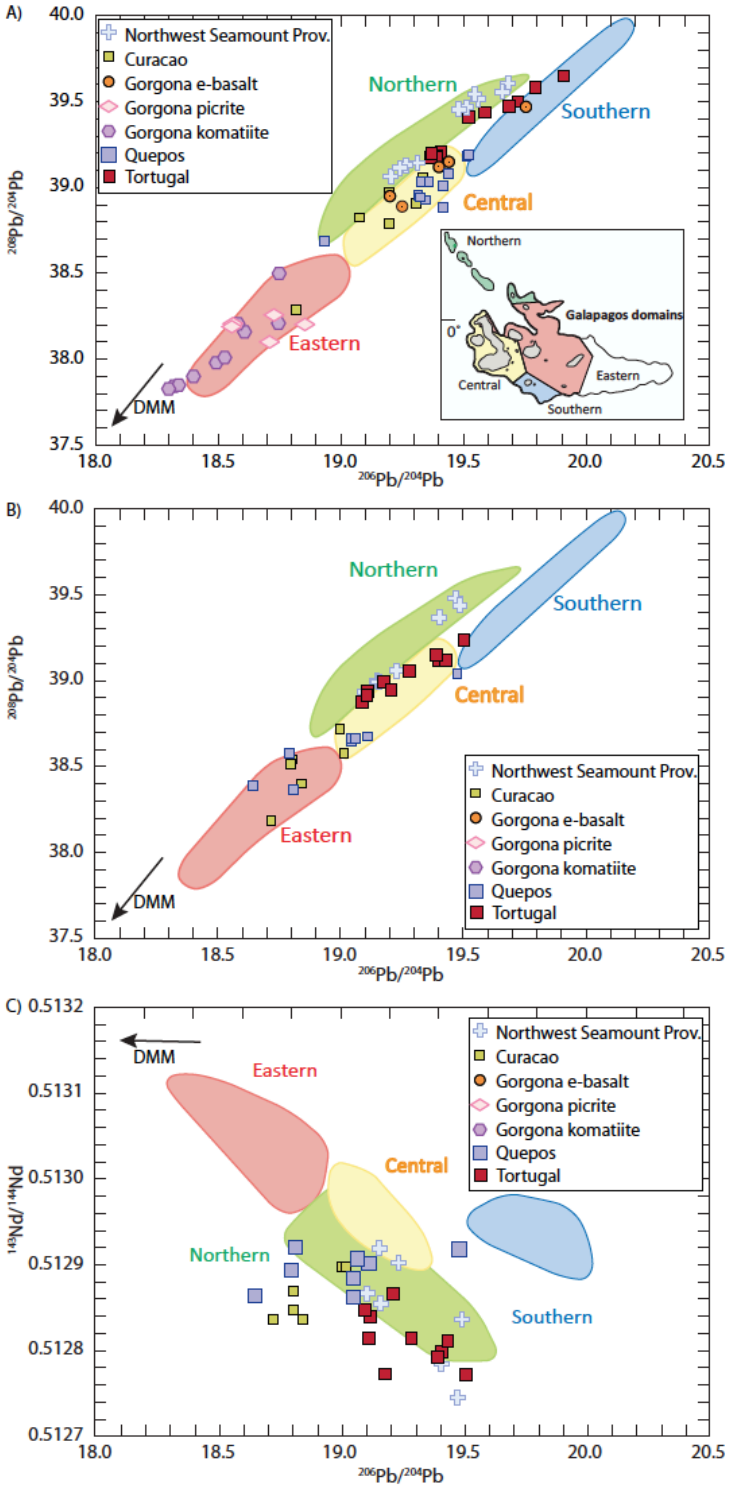

Figure S7: A) Measured $^{208}Pb/^{204}Pb$-$^{206}Pb/^{204}Pb$ radiogenic isotopes. B) Age corrected $^{208}Pb/^{204}Pb$-$^{206}Pb/^{204}Pb$ radiogenic isotopes. Tortugal, Gorgona, and Curacao corrected to 90 Ma. Quepos corrected to 65 Ma. Samples from the Northwest Seamount Province of the Cocos Ridge corrected to 15 Ma. C) Age corrected $^{143}Nd/^{144}Nd$-$^{206}Pb/^{204}Pb$ radiogenic isotopes. DMM=Depleted MORB mantle.

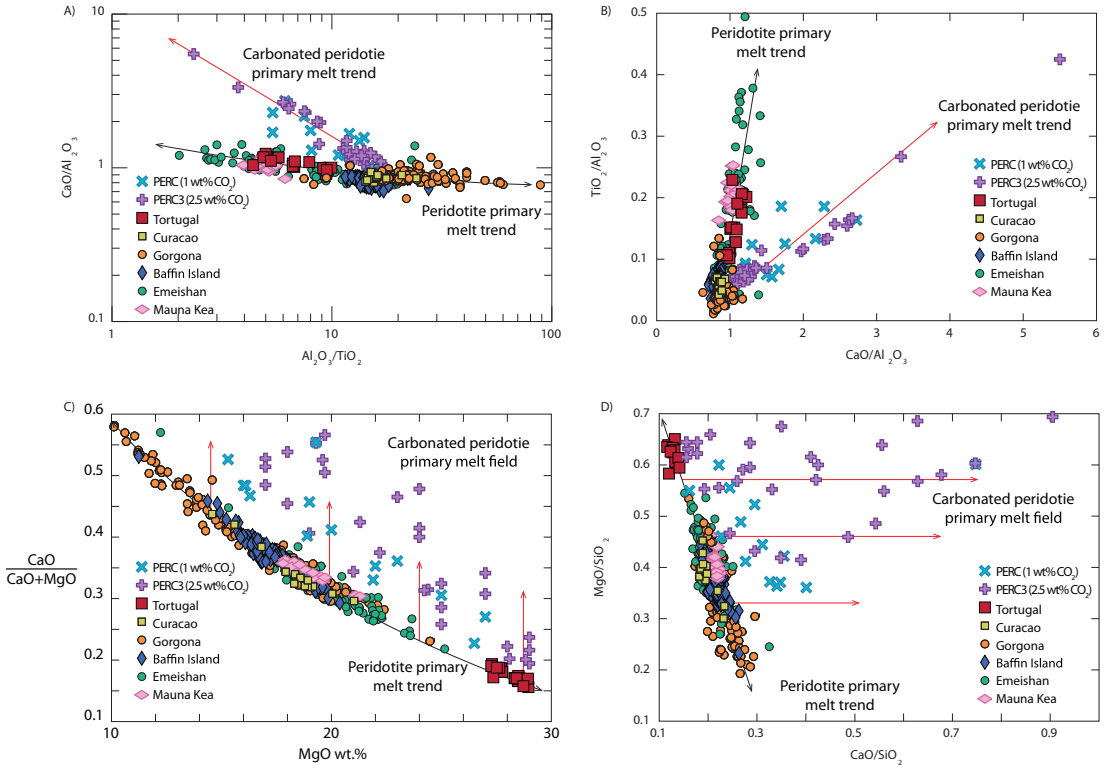

Figure S8: Discrimination diagrams highlighting differences in major element ratios in primary melts between carbonated melting experiments of Dasgupta et al. (2007) and our calculated primary melt compositions for lavas from non-carbonated sources.

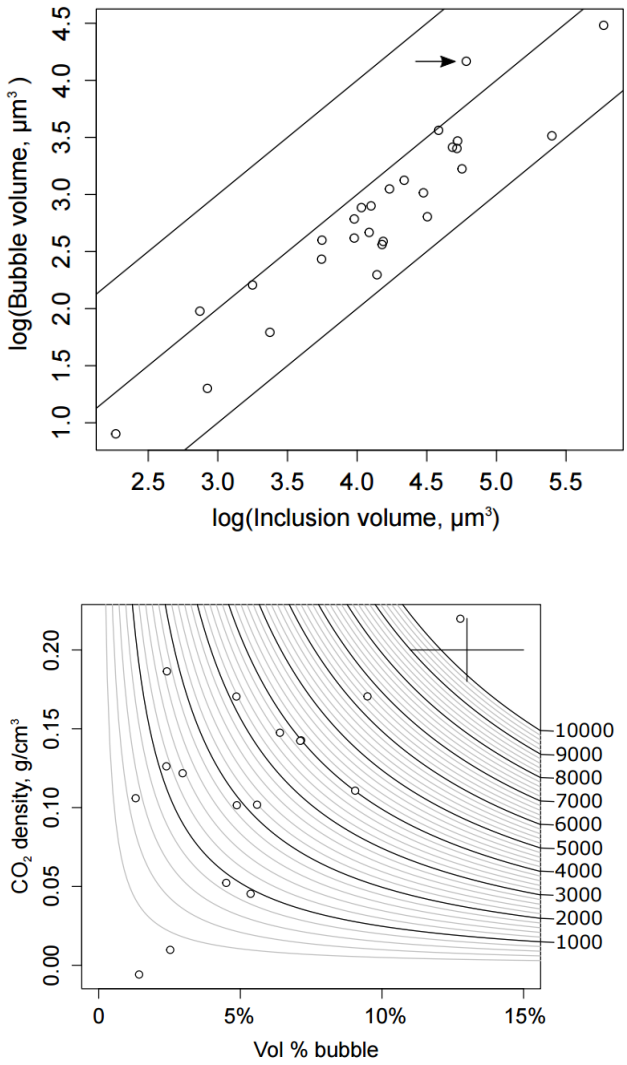

Figure S9: A) Melt inclusion volume versus vapor bubble volume for olivine-hosted melt inclusions in sample TO-080714-8. Contours show volume percent vapor. With the exception of one outlier (arrow), vapor bubble volumes are relatively constant suggesting that vapor bubbles formed after trapping. B) Volume fraction, CO_2 density, and calculated CO_2 concentration for bubbles in olivine-hosted melt inclusions from sample TO-080714-8. Contours show calculated CO_2 content based on bubble volume, bubble density, and an assumed bulk glass density of 2.75 g/cm^3. Average uncertainty is shown with error bars in the upper right corner of the figure.

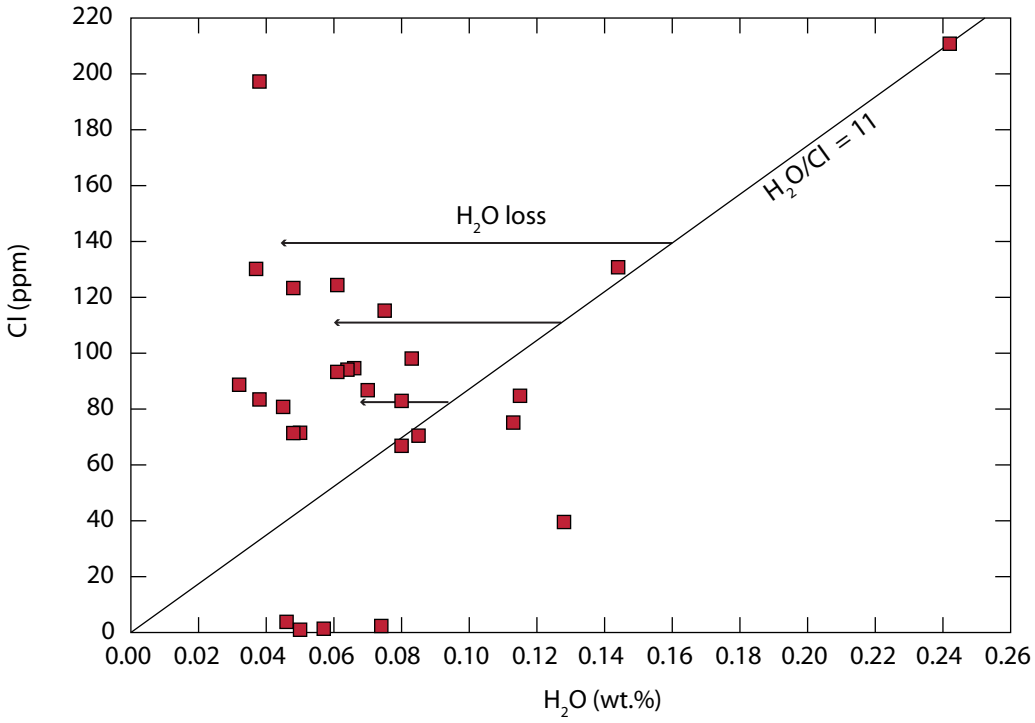

Figure S10: H_2O vs Cl. Sloped line represents inferred covariation between the two elements without water loss. Tortugal olivine-hosted melt inclusions partially degassed. The data suggests approximately 0.24 wt % H_2O in the most pristine melt inclusions that have undergone the least amount of H_2O loss.

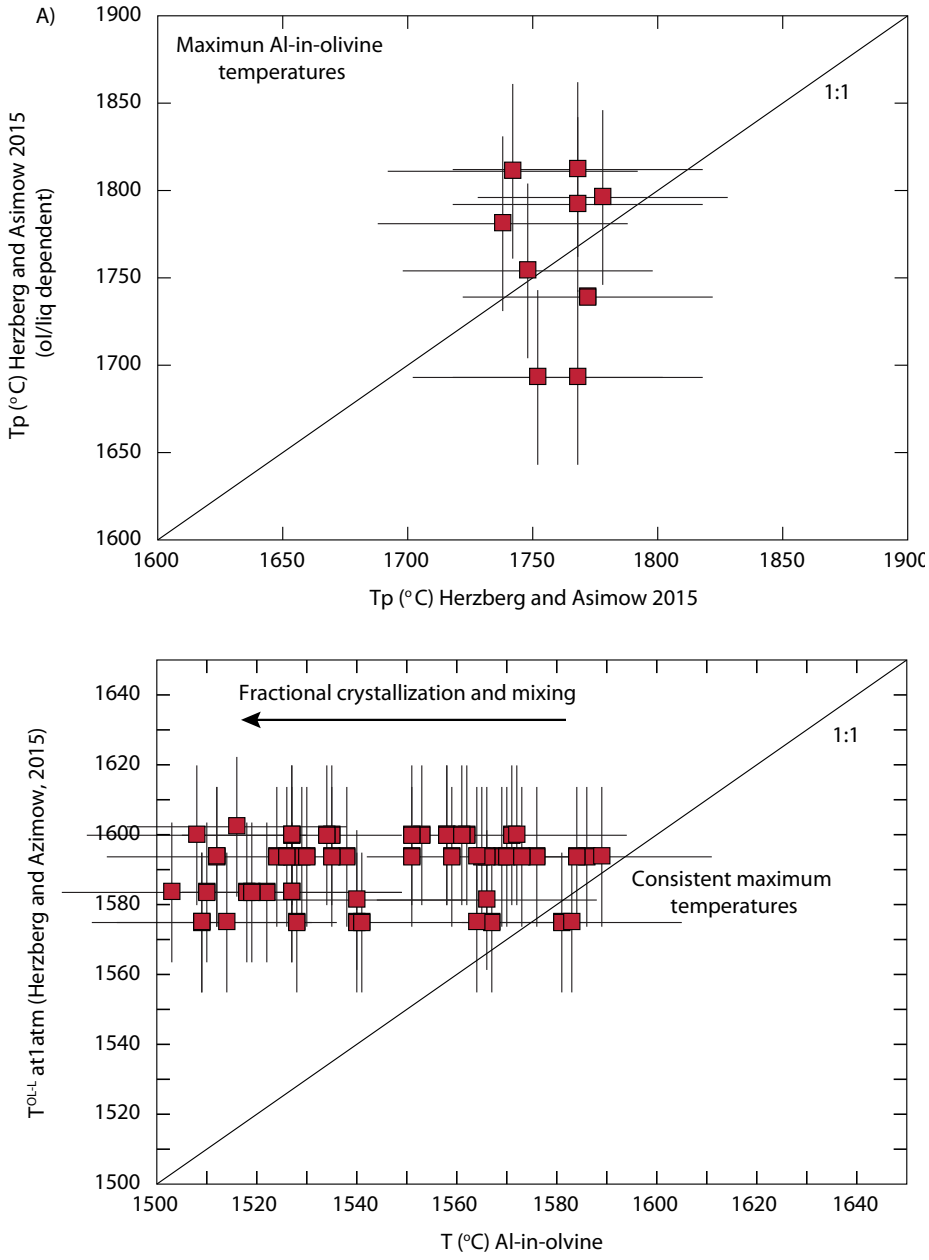

Figure S11: A) A comparison between mantle potential temperature using equations 16 and 17 from Herzberg and Asimow (2015) and maximum temperatures for each respective sample from Al-in-olivine thermometry results. B) A comparison between Al-in-olivine crystallization temperatures and modeled 1 atm olivine liquidus temperatures using equation 13 from Herzberg and Asimow (2015). Error bars = ±22 °C. Maximum Al-in-olivine temperatures correspond (nearly 1:1) with maximum olivine-liquidus temperatures.

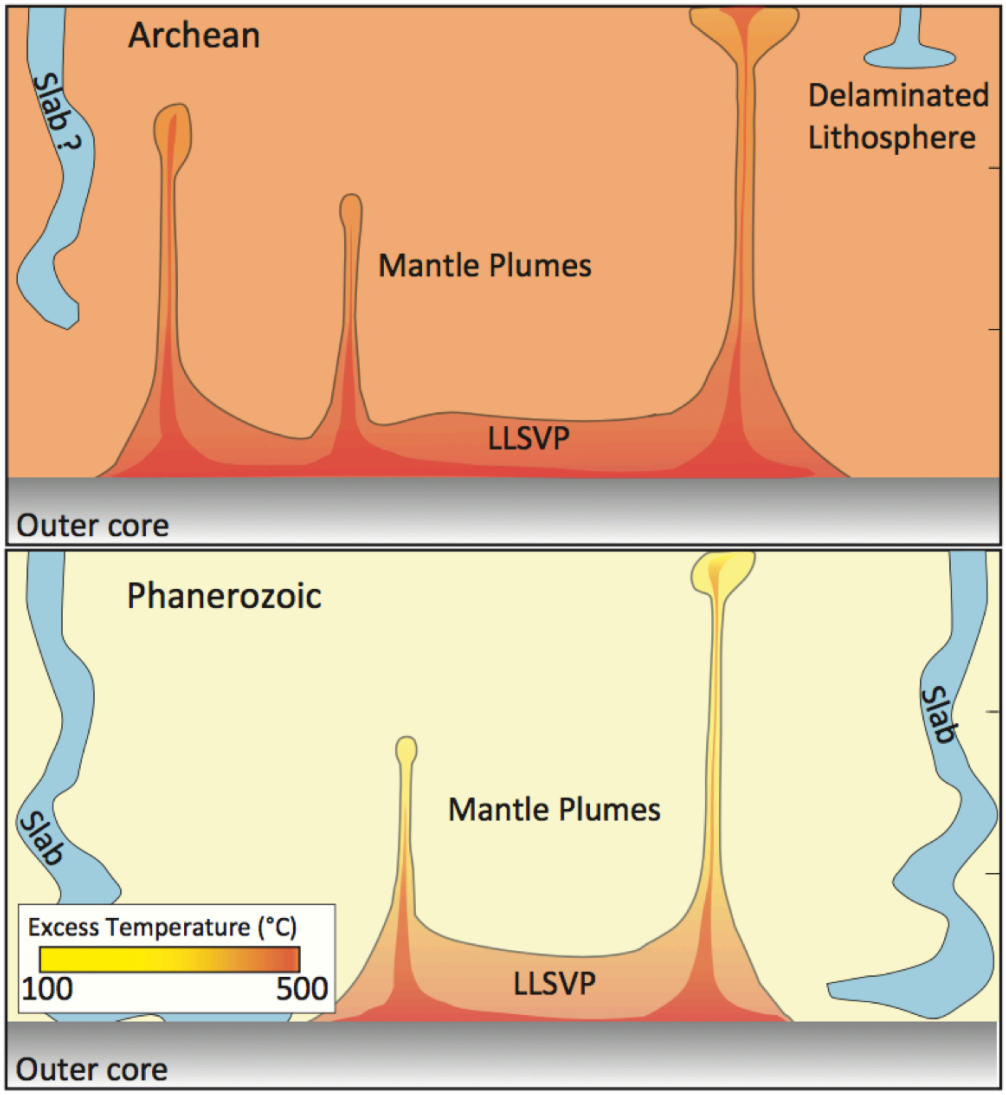

Figure S12: Schematic representation showing the excess temperature of the mantle during the Archean and Phanerozoic relative to modern ambient MORB mantle (1350 °C). Inspired by Garnero et al. (2016).

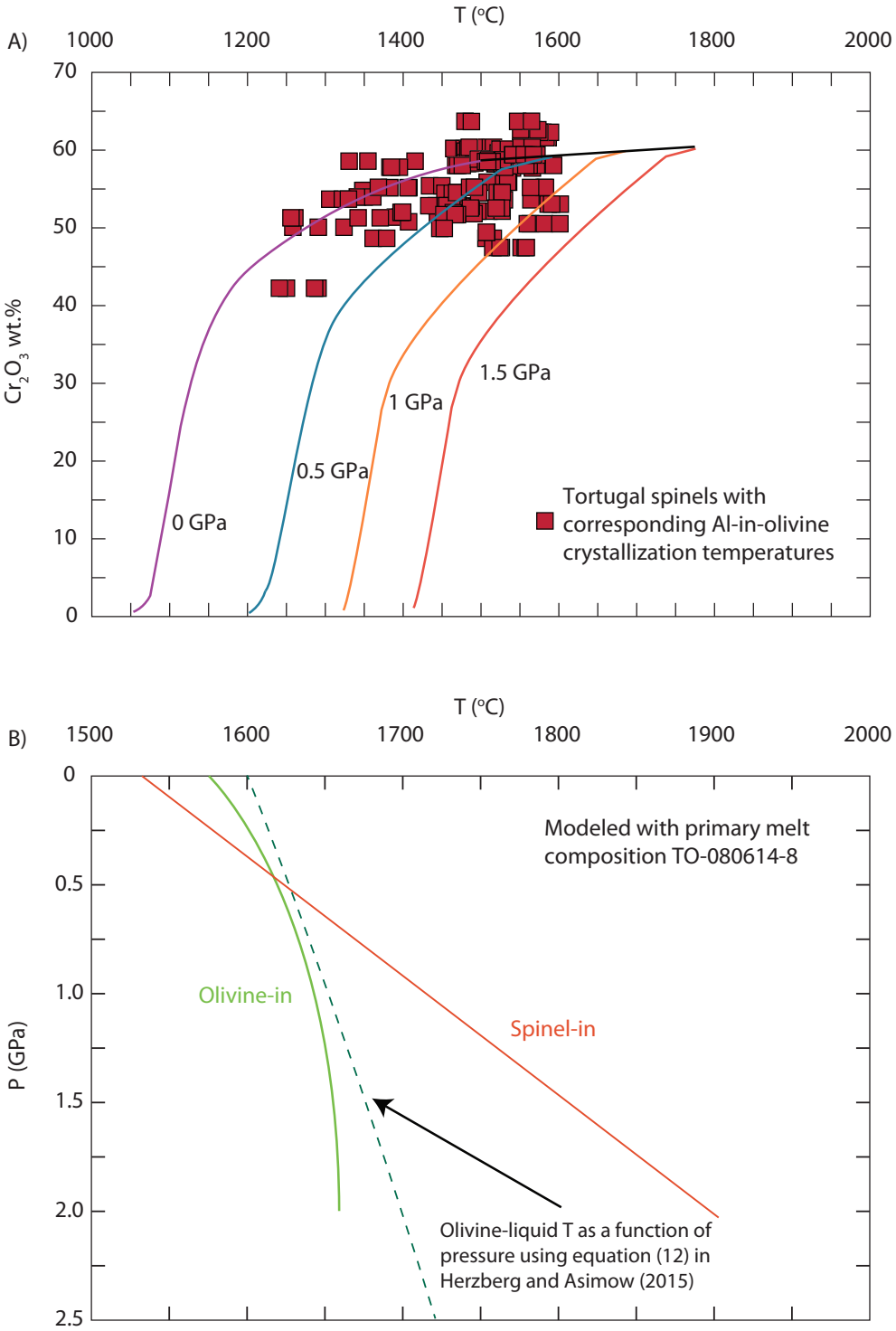

Figure S13: Petrologic models demonstrating the pressure dependence on the spinel-liquidus using the primary magma solution from sample TO-080614-8 as the starting composition. A) Graphical representation of Tortugal spinel compositions and liquid lines of descent modeled with rhyolite-melts software. B) P-T diagram highlighting the pressure dependence on the olivine and spinel liquidus temperatures.

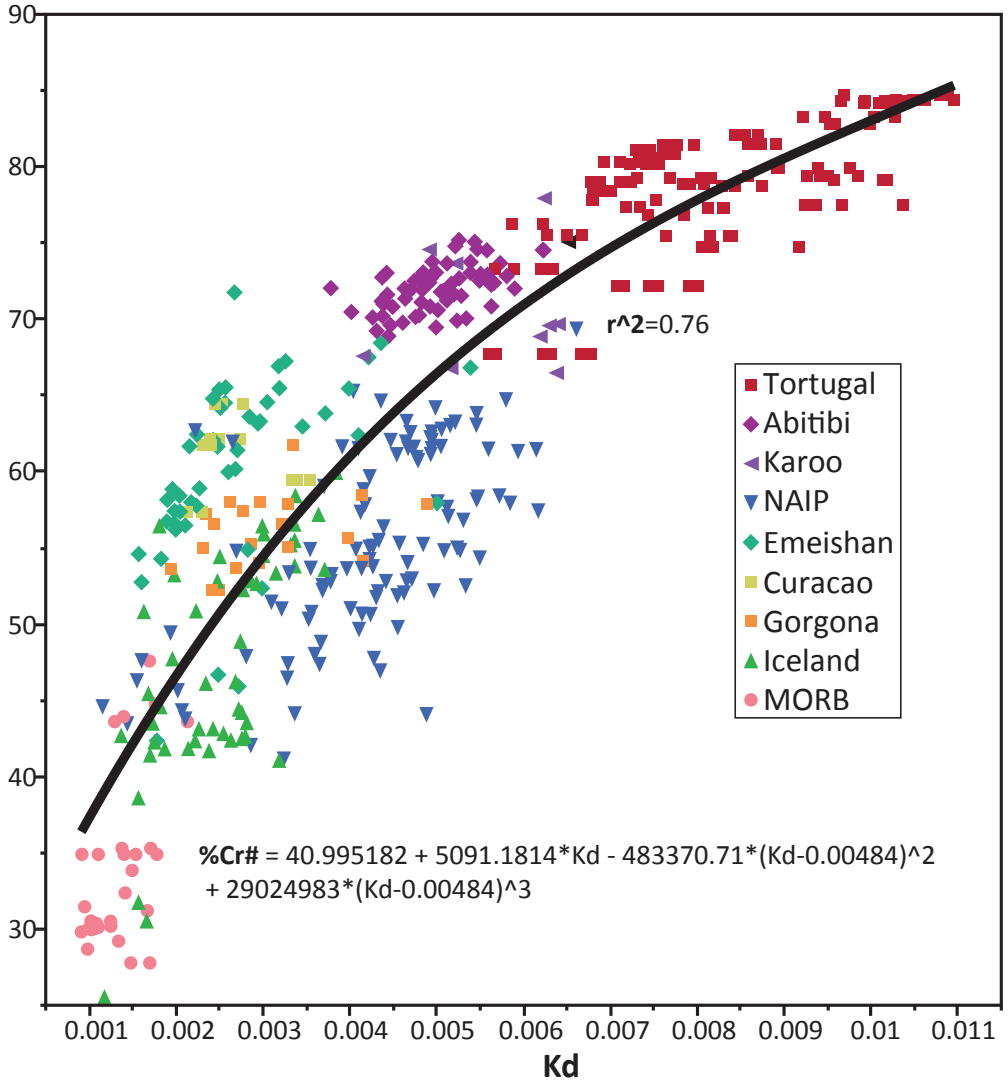

Figure S14: The correlation between Kd (Al2O3 olivine/Al2O3 spinel) and spinel %Cr# (R2=0.75) suggests that the Tortugal olivines analyzed in this study provide statistically meaningful results.

References

Alvarado, G.E., Denyer, P., Sinton, C.W., 1997. The 89 Ma Tortugal komatiitic suite, Costa Rica: Implications for a common geological origin of the Caribbean and Eastern Pacific region from a mantle plume. Geology 25, 439-442.

Andrault, D., Monteux, J., Le Bars, M., Samuel, H., 2016. The deep Earth may not be cooling down. Earth and Planetary Science Letters 443, 195-203.

Arndt, N., 1999. Why was flood volcanism on submerged continental platforms so common in the precambrian? Precambrian Research 97, 155-164.

Arndt, N., 2003. Komatiites, kimberlites, and boninites. Journal of Geophysical Research 108, 2293.

Berry, A.J., Danyushevsky, L.V., O'Neil, H.S.C., Newville, M., Sutton, S.R., 2008. Oxidation state of iron in komatiitic melt inclusions indicates hot Archaean mantle. Nature 455, 960-964.

Danyushevsky, L.V., Plechov, P., 2011. Petrolog3: Integrated software for modeling crystallization processes. Geochemistry, Geophysics, Geosystems 12, n/a-n/a.

Danyushevsky, L.V., Sobolev, A.V., 1996. Ferric-ferrous ratio and oxygen fugacity calculations for primitive mantle-derived melts: calibration of an empirical technique. Mineralogy and Petrology 57, 229-241.

Dasgupta, R., Hirschmann, M.M., Smith, N.D., 2007. Partial Melting Experiments of Peridotite + CO2 at 3 GPa and Genesis of Alkalic Ocean Island Basalts. Journal of Petrology 48, 2093-2124.

Denyer, P., Gazel, E., 2009. The Costa Rican Jurassic to Miocene oceanic complexes: Origin, tectonics and relations. Journal of South American Earth Sciences 28, 429-442.

Dixon, J.E., Leist, L., Langmuir, C.H., Schilling, J.-G., 2002. Recycled dehydrated lithosphere observed in plume-influenced mid-ocean-ridge basalt. Nature 420, 385-389.

Dupré, B., Allegre, C.J., 1983. Pb-SR isotope variation in Indian Ocean basalts and mixing phenomena. Nature 303, 142-146.

Foley, S.F., Prelevic, D., Rehfeldt, T., Jacob, D.E., 2013. Minor and trace elements in olivines as probes into early igneous and mantle melting processes. Earth and Planetary Science Letters 363, 181-191.

Garnero, E.J., McNamara, A.K., Shim, S.-H., 2016. Continent-sized anomalous zones with low seismic velocity at the base of Earth's mantle. Nature Geoscience 9, 481-489.

Gazel, E., Plank, T., Forsyth, D.W., Bendersky, C., Lee, C.-T.A., Hauri, E.H., 2012. Lithosphere versus asthenosphere mantle sources at the Big Pine Volcanic Field, California. Geochemistry Geophysics Geosystems 13.

Grove, T.L., Parman, S.W., Dann, J.C., 1999. Conditions of magma generation for Archean komatiites from the Barberton Mountainland, South Africa, in: Fei, Y., Bertka, C.M., Mysen, B.O. (Eds.), Mantle Petrology: Field Observations and High-Pressure Experimentation. The Geochemical Society, Houston, pp. 155-167.

Gualda, G.A.R., Ghiorso, M.S., Lemons, R.V., Carley, T.L., 2012. Rhyolite-MELTS: A modified calibration of MELTS optimized for silica-rich, fluid-bearing magmatic systems. Journal of Petrology 53, 875-890.

Hanski, E., 1992. Petrology of the Pechenga ferropicrites and cogenetic, Ni-bearing gabbro-wehrlite intrusions, Kola Peninsula, Russia. Geological Survey of Finland Bulletin 367.

Harpp, K.S., White, W.M., 2001. Tracing a mantle plume: Isotopic and trace element variations of Galapagos seamounts. Geochemistry Geophysics Geosystems 2, 1525.

Hart, S.R., 1984. A large-scale isotope anomaly in the Southern Hemisphere mantle. Nature 309, 753-757.

Hartley, M.E., Maclennan, J., Edmonds, M., Thordarson, T., 2014. Reconstructing the deep CO2 degassing behaviour of large basaltic fissure eruptions. Earth and Planetary Science Letters 393, 120-131.

Hauff, F., Hoernle, K., Van den Bogaard, P., Alvarado, G., Garbe-Schönberg, D., 2000. Age and geochemistry of basaltic complexes in western Costa Rica: Contributions to the geotectonic evolution of Central America. Geochemistry Geophysics Geosystems.

Herzberg, C., 1992. Depth and degree of melting of Komatiites. Journal of Geophysical Research 97, 4521-4540.

Herzberg, C., 2016. Petrological Evidence from Komatiites for an Early Earth Carbon and Water Cycle. Journal of Petrology 57, 2271-2288.

Herzberg, C., Asimow, P.D., 2015. PRIMELT3 MEGA.XLSM software for primary magma calculation: Peridotite primary magma MgO contents from the liquidus to the solidus. Geochemistry Geophysics Geosystems 16.

Herzberg, C., O'Hara, M.J., 2002. Plume-Associated Ultramafic Magmas of Phanerozoic Age. Journal of Petrology 43, 1857-1883.

Hofmann, A., 1997. Mantle geochemistry: the message from oceanic volcanism. Nature 385, 219-229.

Kerr, A.C., Arndt, N.T., 2001. A Note on the IUGS Reclassification of the High-Mg and Picritic Volcanic Rocks. Journal of Petrology 42, 2169-2171.

Li, Z.-X.A., Lee, C.-T.A., 2004. The constancy of upper mantle fO2 through time inferred from V/Sc ratios in basalts. Earth and Planetary Science Letters 228, 483-493.

Lofgren, G.E., 1983. Effect of Heterogeneous Nucleation on Basaltic Textures: A Dynamic Crystallization Study. Journal of Petrology 24, 229-255.

McDonough, W.F., Sun, S.-s., 1995. The composition of the Earth. Chemical Geology 120, 223-253.

Michael, P.J., Graham, D.W., 2015. The behavior and concentration of CO2 in the suboceanic mantle: Inferences from undegassed ocean ridge and ocean island basalts. Lithos 236-237, 338-351.

Moore, L.R., Gazel, E., Tuohy, R., Lloyd, A.S., Esposito, R., Steele-MacInnis, M., Hauri, E.H., Wallace, P.J., Plank, T., Bodnar, R.J., 2015. Bubbles matter: An assessment of the contribution of vapor bubbles to melt inclusion volatile budgets. American Mineralogist 100, 806-823.

Parman, S., Grove, T.L., Dann, J., 2001. The production of Barberton komatiites in an Archean subduction zone. Geophysical Research Letters 28, 2513-2516.

Putirka, K.D., Perfit, M., Ryerson, F.J., Jackson, M.G., 2007. Ambient and excess mantle temperatures, olivine thermometry, and active vs. passive upwelling. Chemical Geology 241, 177-206.

Sobolev, A., Batanova, V., Asafov, E., Gurenko, A.A., Arndt, N., Krasheninnikov, S., Portnyagin, M., Garbe-Schönberg, D., 2015. How Hot and Wet are Mantle Derived Magmas and Their Sources? AGU Fall Meeting.

Sobolev, A.V., Asafov, E.V., Gurenko, A.A., Arndt, N.T., Batanova, V.G., Portnyagin, M.V., Garbe-Schonberg, D., Krasheninnikov, S.P., 2016. Komatiites reveal a hydrous Archaean deep-mantle reservoir. Nature 531, 628-632.

Sossi, P.A., Eggins, S.M., Nesbitt, R.W., Nebel, O., Hergt, J.M., Campbell, I.H., O'Neill, H.S.C., Van Kranendonk, M., Davies, D.R., 2016. Petrogenesis and Geochemistry of Archean Komatiites. Journal of Petrology 57, 147-184.

Tenner, T.J., Hirschmann, M.M., Humayun, M., 2012. The effect of H2O on partial melting of garnet peridotite at 3.5 GPa. Geochemistry, Geophysics, Geosystems 13, n/a-n/a.

Trela, J., Vidito, C., Gazel, E., Herzberg, C., Class, C., Whalen, W., Jicha, B., Bizimis, M., Alvarado, G.E., 2015. Recycled crust in the Galápagos Plume source at 70 Ma: Implications for plume evolution. Earth and Planetary Science Letters 425, 268-277.

Walter, M.J., 1998. Melting of Garnet Peridotite and the Origin of Komatiite and Depleted Lithosphere. Journal of Petrology 39, 29–60.

Tortugal Atlas

Images of olivine, inclusions, and chemical maps

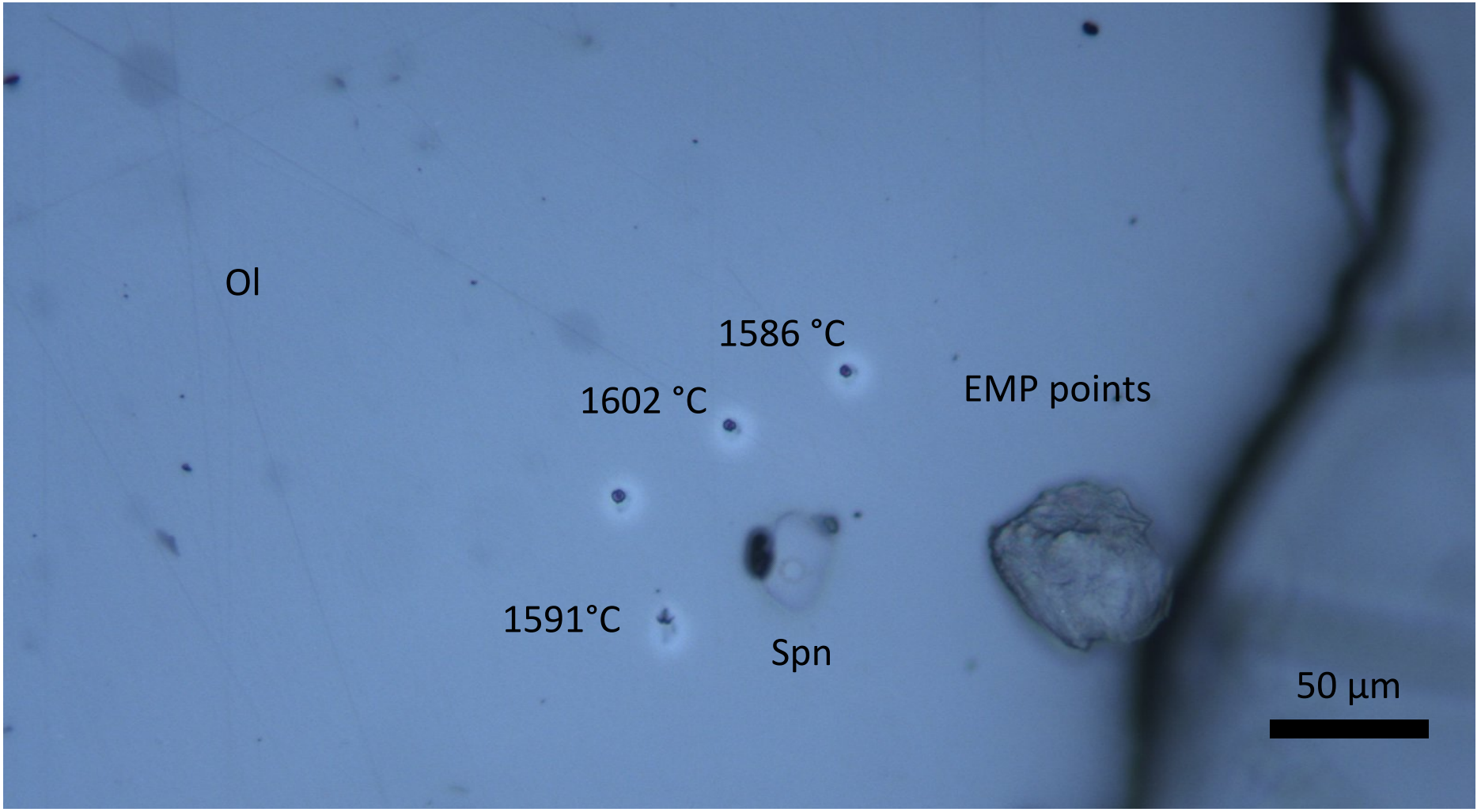

Atlas Figure 1: Euherdral spinel crystal in olivine phenocryst. TO-080514-1-7. Max Mg#=93.32. Reflected light

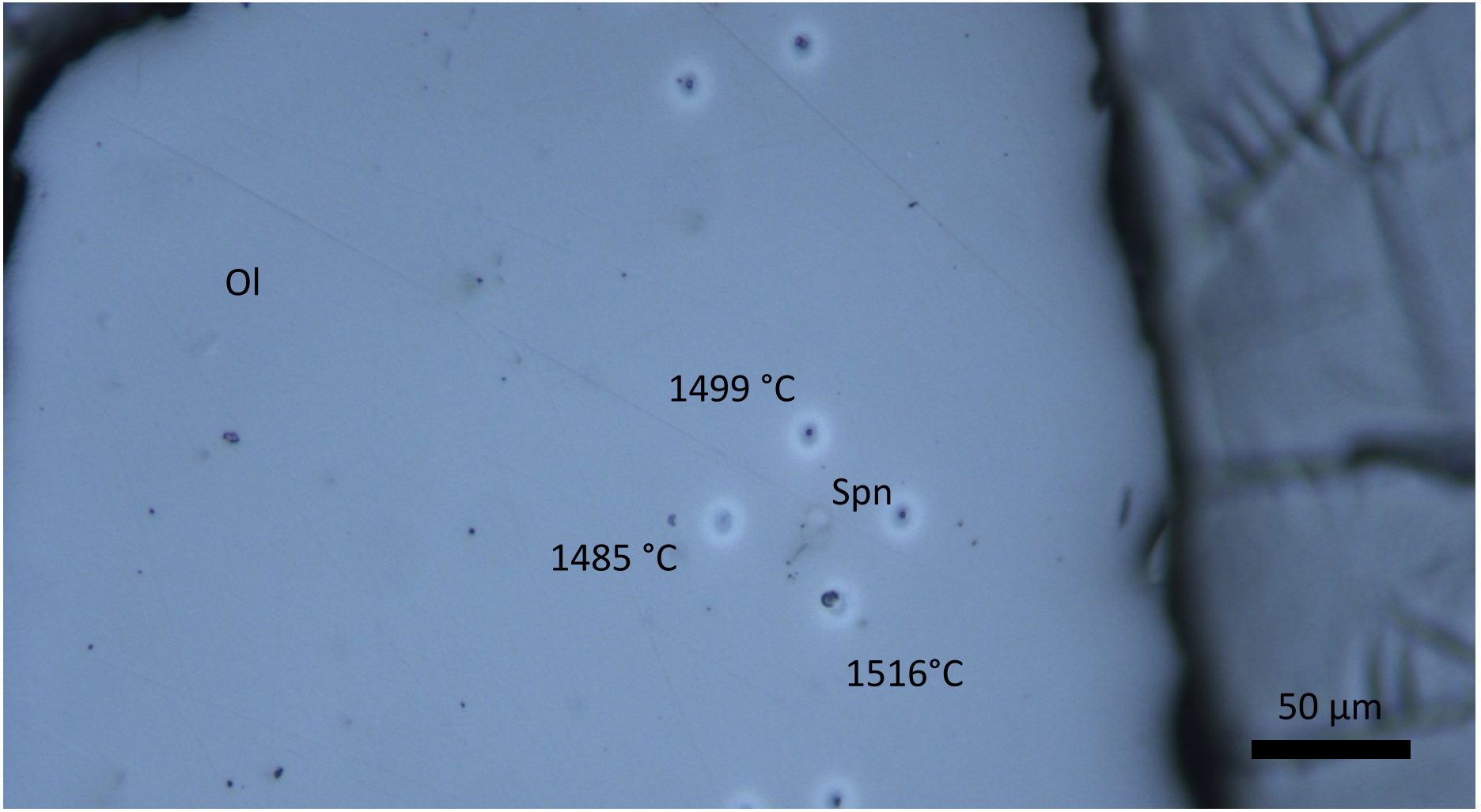

Atlas Figure 2: Spinel inclusions in primitive Tortugal olivine. TO-080514-1-31. Max Mg#=93.24. Reflected light. White halos around spinel inclusions are microprobe analyses.

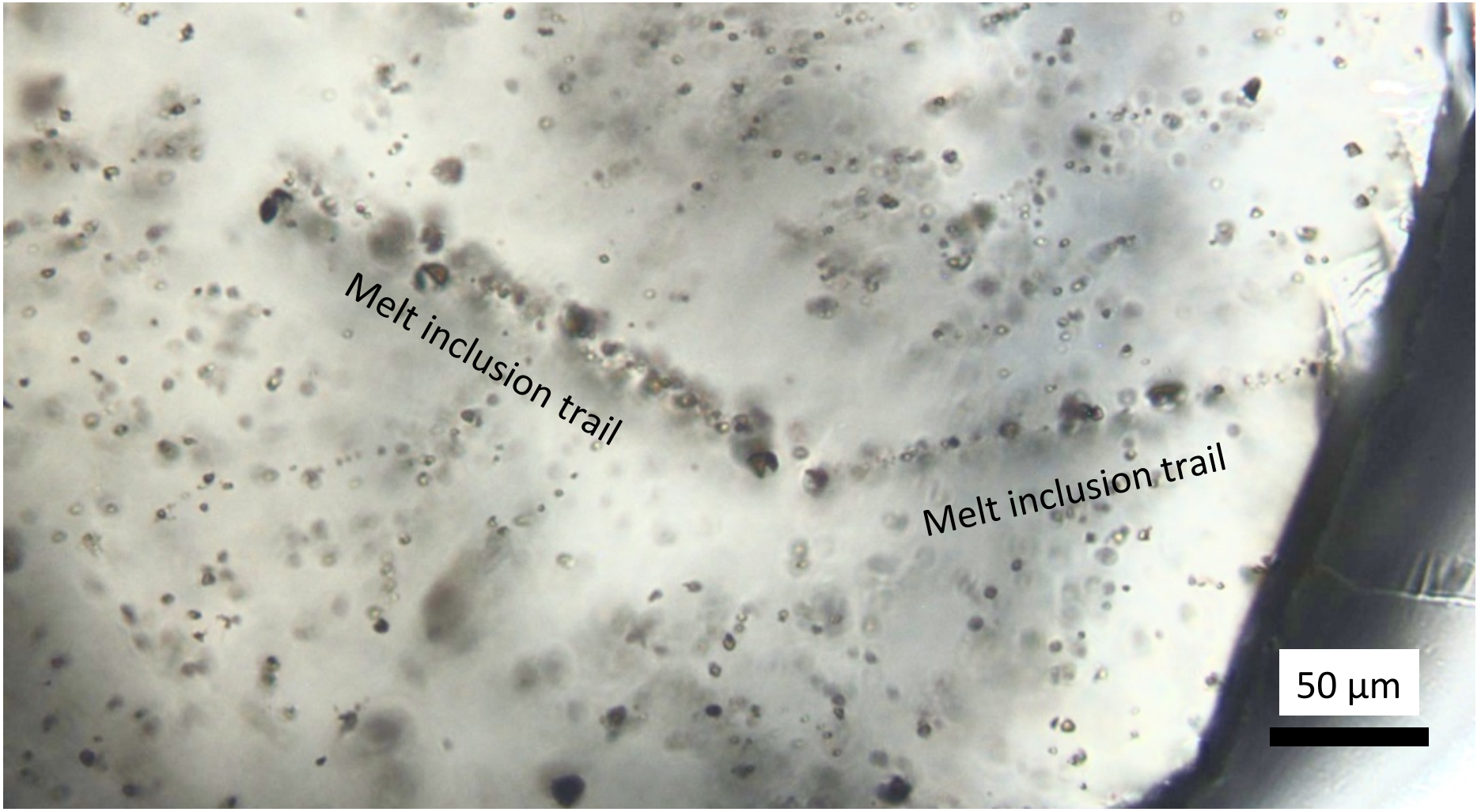

Atlas Figure 3: Trail of melt inclusions in primitive Tortugal olivine. TO-080514-8-13. Max Mg#=93.90. Transmitted light.

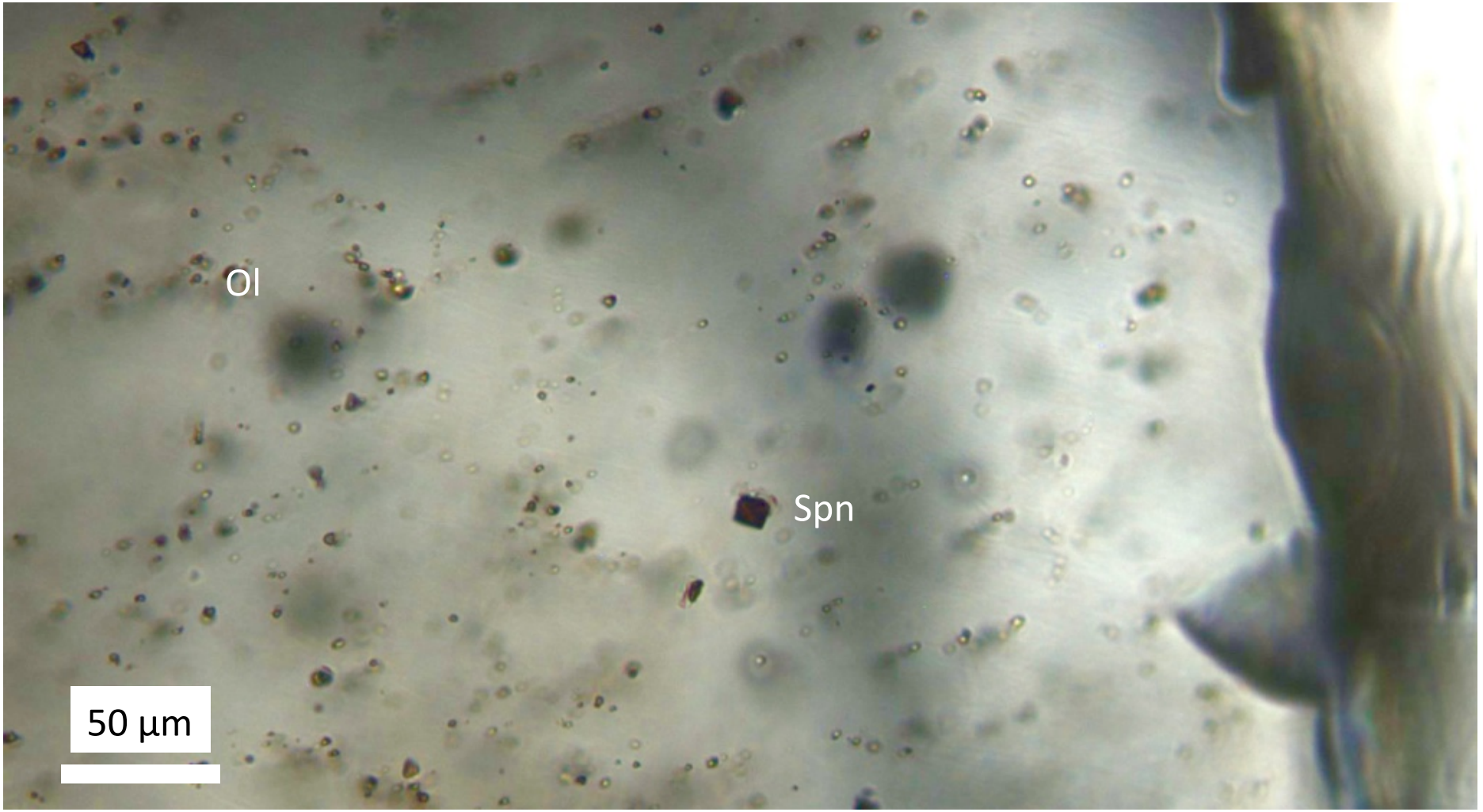

Atlas Figure 4: Euherdral spinel inclusion in primitive Tortugal olivine. TO-080514-8-13. Max Mg#=93.90. Transmitted light.

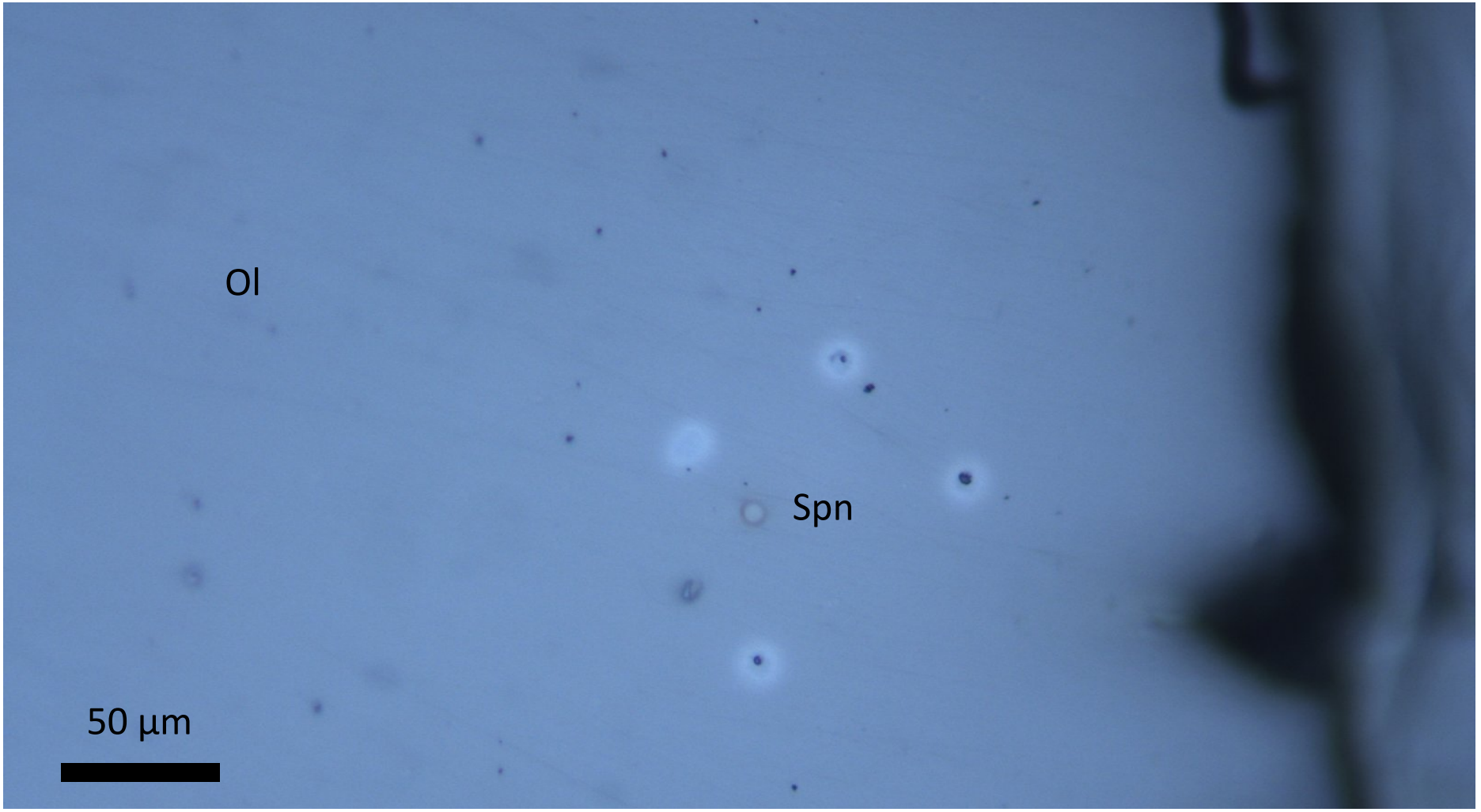

Atlas Figure 5: Euherdral spinel inclusion in primitive Tortugal olivine. TO-080514-8-13. Max Mg#=93.90. Transmitted light.

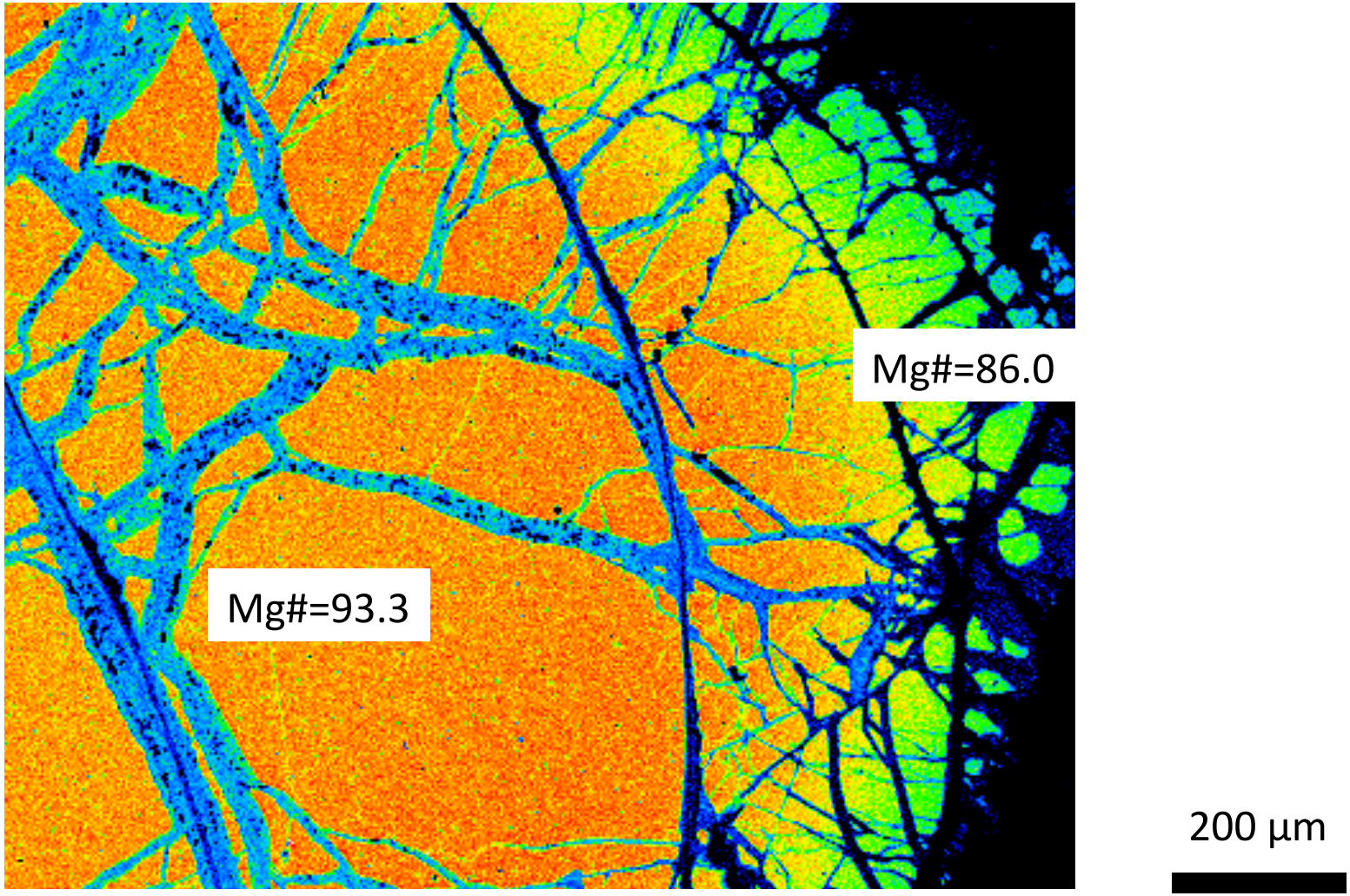

Atlas Figure 6: EDS chemical map of Tortugal olivine in thin-section showing distribution of Mg and normal magmatic zonation. Sample TO-080714-8.

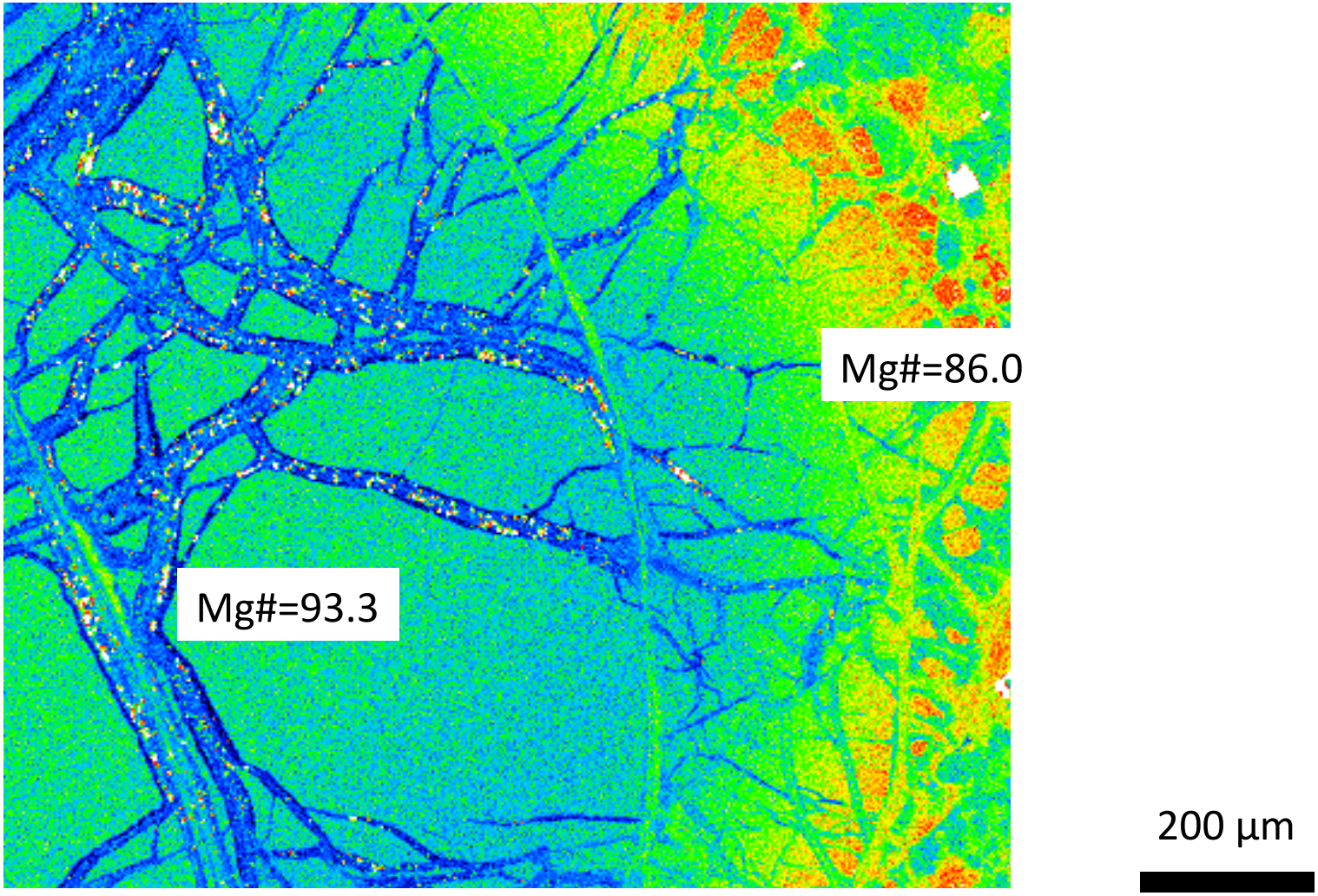

Atlas Figure 7: EDS chemical map of Tortugal olivine in thin-section showing distribution of Fe and normal magmatic zonation. Sample TO-080714-8.

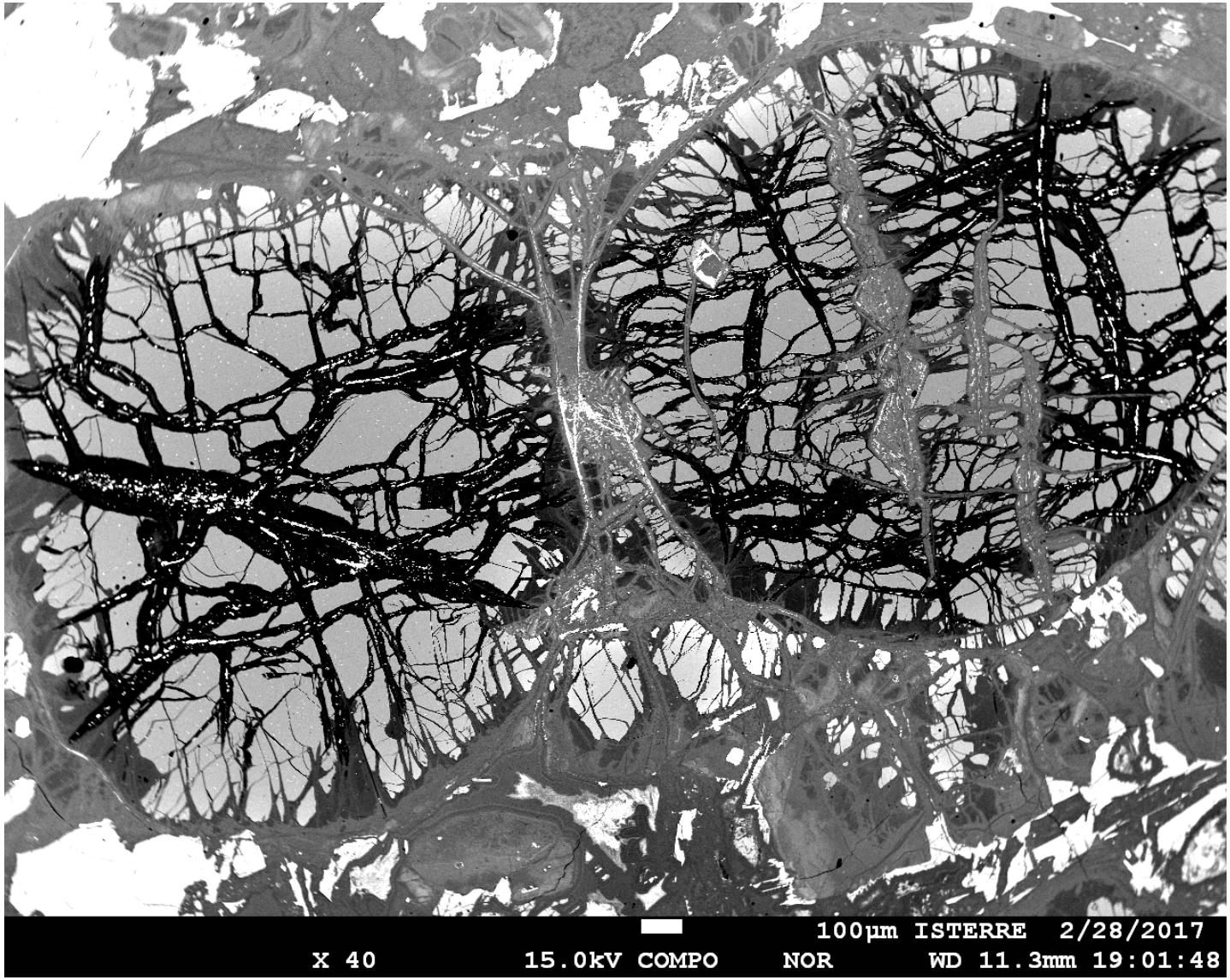

Atlas Figure 8: Backscattered electron image of two euhedral high-Mg olivine grains in sample TO-080514-3. The cores have compositions Mg# 92.4 (right) and Mg#92.1 (left), while their rims have Mg# down to 86

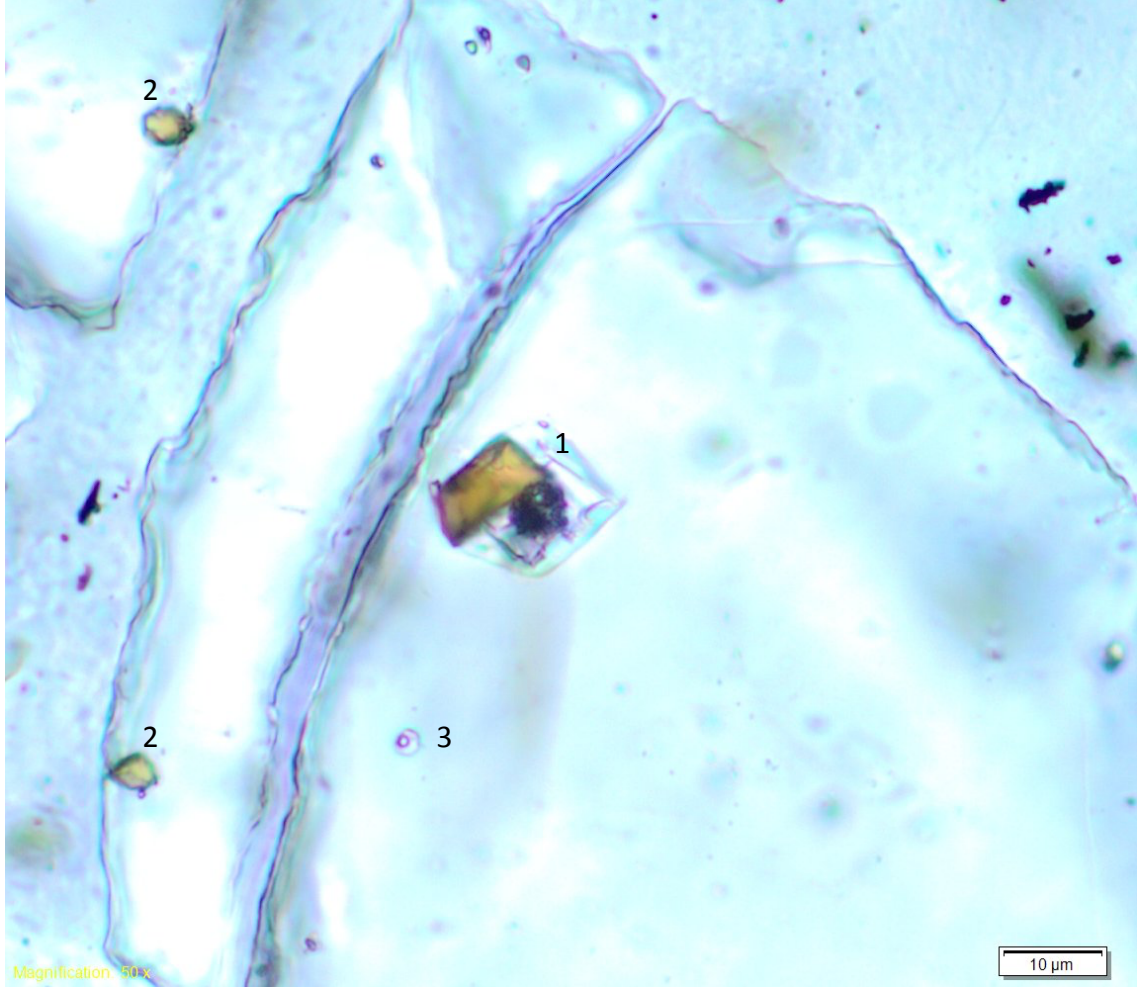

Extended Data Figure 9: Optical image of core of an olivine (Mg# 92.9, Al_2O_3=0.0744) sample TO-080514-3, containing combined melt inclusion (1) with spinel grain (brown), gas bubble, crystals and glass. The same grain contains inclusions of single spinel (2) and glass with gas bubble (3). The relatively large size of spinel in the inclusion 1 suggests that it was trapped as a crystal together with melt. Presence of the combined spinel-melt inclusions, single spinel crystals and melt, and the homogenous composition of the olivine core indicates equilibrium of olivine, spinel and melt during crystallization of high-Mg olivine and confirms application of olivine-spinel geothermometry. **Temperature calculated for this particular grain (Coogan et al, 2014) corresponds to 1550±7°C).**